Universidade de Aveiro
Ano 2023

Nuno Fonseca Valente

Pós-processamento de fibras óticas para aplicações de sensores

Optical fiber post-processing techniques for sensor applications

Universidade de Aveiro
Ano 2023

Nuno Fonseca Valente

Pós-processamento de fibras óticas para aplicações de sensores

Optical fiber post-processing techniques for sensor applications

Dissertação apresentada à Universidade de Aveiro para cumprimento dos requisitos necessários à obtenção do grau de Mestre em Engenharia Física, realizada sob a orientação científica do Doutor Ricardo Jorge Figueiredo Oliveira, e coorientação da Doutora Lúcia Maria Botas Bilro, investigadores do Instituto de Telecomunicações.

Dedico este trabalho a todos os que me apoiaram nesta etapa turbulenta que foi a Universidade. A todos vocês que sempre me apoiaram, vocês sabem quem são, só quero dizer que vos adoro e agradeço-vos do fundo do coração esse apoio constante.

o júri / the jury

	Professora Doutora Margarida Maria Resende Vieira Facão Professora Auxiliar Universidade de Aveiro
vogais / examination committee	Professor Doutor Manuel Filipe Pereira da Cunha Martins Costa Professor Auxiliar da Universidade do Minho
	Doutor Ricardo Jorge Figueiredo Oliveira Investigador do Instituto de Telecomunicações (orientador)

agradecimentos/ acknowledgments

Começo por agradecer aos meus orientadores, o professor Ricardo Oliveira e a professora Lúcia Bilro, pelo apoio incansável que me deram ao longo da tese, estando sempre dispostos para me tirar quaisquer dúvidas que surgissem e por me darem a oportunidade de continuar a trabalhar na área da ótica. Gostaria também de agradecer ao professor Flávio Figueira por me auxiliar no processo de corrosão das fibras óticas de vidro, sem o seu contributo não teria sido possível realizar parte do trabalho descrito nesta tese. Gostaria de agradecer também à minha família, que desde sempre me apoiou em todas as decisões e etapas que surgiram ao longo da minha vida, não sendo a tese a exceção a esse apoio constante. Gostaria também de agradecer a todos os meus amigos, os quais me suportaram ao longo do meu percurso académico e sem os quais muito provavelmente não estaria a apresentar a tese nesta altura. Por fim, gostaria de agradecer ao Instituto de Telecomunicações e ao projeto FOPE-ComSens (PTDC/EEI-TEL/1511/2020) pelas condições proporcionadas que permitiram a realização desta tese.

palavras-chave

Sensores de fibra ótica, interferometros multimodais, redes de período longo, pressão hidrostática, deformação, deslocamento, temperatura, filtros espectrais

resumo

Neste trabalho são propostas técnicas de pós-processamento de fibras óticas com o intuito de produzir sensores de fibra ótica de fácil fabrico, com baixo custo e com características competitivas comparadas com os demais sensores. O primeiro dispositivo baseou-se em interferómetros multimodais. Estes foram feitos através da fusão de fibras óticas multimodo tanto de vidro (GOF) como de polímero (POF) entre duas fibras óticas monomodo de vidro. Para o sensor à base de GOF foi obtida uma sensibilidade de 4.6 pm/bar. Já para o interferómetro multimodal baseado em POF, foi obtida uma sensibilidade de 58 pm/bar, que corresponde a uma melhoria da sensibilidade de doze vezes quando comparada com o sensor baseado em GOF. Além disso, esta é cinco vezes superior à obtida para tecnologia de redes de Bragg em POF. Esta melhoria na sensibilidade torna este sensor muito promissor, uma vez que permite obter resoluções muito maiores.

O segundo sensor de fibra ótica abordado neste trabalho consistiu em redes de período longo mecanicamente induzidas. Estas foram obtidas através de metodologias de simples fabricação, que consistiam em distribuir periodicamente resina fotopolimerizável numa GOF-monomodo, seguido de um processo de corrosão química que permitiu modular periodicamente o diâmetro da fibra. Este método de produção é muito mais vantajoso comparado com os seus rivais diretos, uma vez que aplica técnicas de produção baratas e de simples reprodução, não exigindo a utilização de tecnologias de fotolitografia ou de deposição química de vapor. A caraterização desta estrutura a parâmetros externos, tais como: tensão longitudinal, deslocamento e temperatura revelaram capacidades promissoras, uma vez que permitiram não só a sintonização da banda espetral tanto em comprimento de onda como também em potência ótica de acoplamento. Os resultados foram bastante promissores no que concerne às caraterizações do deslocamento, uma vez que se obteve uma gama de medição de 0 - 60 mm, o que é maior que aquelas reportadas na literatura (i.e. até 2 mm).

keywords

Optical fiber sensors, multimodal interferometers, long period gratings, hydrostatic pressure, strain, displacement, temperature, spectral filters

abstract

In this work optical fiber post-processing techniques are proposed in order to produce optical fiber sensors (OFS) with lower costs, simplicity and with competitive characteristics compared with their counterparts. The first device was based on multimode interferometers. Those were fabricated by fusing multimode (MM) glass silica fibers (GOF) and MM polymer optical fibers (POF) between two single mode GOFs. For the GOF-based sensor, it was obtained a sensitivity of 4.6 pm/bar. Regarding the POF-based multimodal interferometer, a sensitivity of 58 pm/bar was reached, which corresponds to an enhancement of the sensitivity of twelve times when compared to the one obtained for GOF. Additionally, this sensitivity is five times higher than the one obtained for the POF Bragg grating technology. This improvement in sensitivity makes this sensor very promising since it can reach higher resolutions.

The second fiber optic sensor discussed in this work consisted of mechanically induced long period gratings. These were obtained through very simple fabrication methodologies, which consisted of a periodical distribution of photopolymerizable resin onto a single mode GOF, followed by chemical corrosion, which allowed to periodically modulate the fiber diameter. This production method is more advantageous than its direct rivals since it applies cheap and easy to reproduce production techniques and does not require the use of photolithography or chemical vapor deposition technologies. The characterization of this structure to external parameters, such as: longitudinal strain, displacement and temperature revealed promising capabilities, since they allowed, not only the wavelength tuning of the spectral band, but also the optical power coupling strength. The results were very promising, as far as the displacement characterizations are concerned, since a measurement range of 0 - 60 mm was obtained, which is larger than those reported in the literature (i.e. up to 2 mm).

Table of contents

1. Introduction

1.1. Motivation and outline

Nowadays optical fibers play an important role in our society and are present in our everyday activities. As examples, optical fibers are the root of our communication systems, but they have also other interesting field of applications, such as in lightning, and or in sensor applications.

Optical fibers have been used to transmit information in long-distance communications due to their low transmission losses (0.2 dB/km). Furthermore, they present other advantages such as high bandwidths, allowing to transmit large amounts of data at a higher rates, they have immunity to electromagnetic interference (EMI), making them a reliable link for data transmission in noisy environments and offering at the same time a secure way to transmit information [1].

Despite its wide use in data transmission, optical fibers also offer attractive characteristics in sensor applications. Examples of that are associated to their multiplexing capabilities, allowing to have multiple sensors distributed along the same fiber cable, they are also lightweight and have small size (125 µm diameter), making it easy to install, finally, they are also robust and resilient, allowing to withstand in harsh environments such as the ones found in the gas and oil industries and in marine environments [2]. These attributes allow their implementation in different fields. One example is in aerospace industry, namely for the structural health monitoring of airplanes [3], enabling a reduction on the maintenance costs and an easier way to monitor its integrity. Another example is found in medicine, namely for the detection of human movement, which can be helpful to track the patient's physical activity levels and consequently improve their rehabilitation program [4].

One of the most studied parameters involving optical fibers is the pressure sensing [5]. This occurs due to its wide range of applications. Examples are down-hole pressure measurements [6], to measure the depth in oceans [7], hydrostatic pressure [8] and blood pressure [9]. Because of that, different fiber optic schemes have already been implemented. Examples are found in the grating technology, as is the case of fiber Bragg gratings (FBGs) [10]; or in the form of fiber optic interferometers, such as, Fabry-Perot interferometers (FPIs) [11], [12]. Despite this wide variety of optical fiber sensors (OFS), their fabrication is normally expensive and involves complex fabrication techniques, since it requires the use of costly equipment, as is the case of CO_2 lasers, ultraviolet (UV) lasers, femtosecond lasers, etc. That equipment also requires personnel with specialized skill which is a downside regarding their use. Because of that, simpler fabrication and lower cost technologies are more attractive. One technology that fits these criteria is multimodal interferometers (MMIs). This occurs, because MMIs offer simple production processes, since it only consists in the fusion of a multimodal fiber between two single mode fibers. MMIs have the ability to measure a wide range of parameters such as strain [13], temperature [14], torsion [15], curvature [16], among others [17]. Despite this wide versatility, the only report of an MMI able to measure hydrostatic pressure has only been reported by Chen et al. [18]. The interferometer was based on a few-mode glass optical fiber

sandwiched between two SMFs, in which the sensitivity reported was about −2.4 pm/bar. Considering that standard fiber optic interrogators operate with resolutions of 5 pm, this leads to a detection limit of 2.1 bar, which is low for most of standard pressure applications.

Nowadays a variety of works report the use of POFs instead of GOFs in optical fiber sensors. The reason relates to the higher sensitivities that could be reached and due to the special properties of POFs. Those include a higher elastic limit (10 % for the POF vs. 1% for the GOF), a 23 times lower Young's modulus, a lower Poisson's ratio (~0.35 vs. ~0.17, for the POF and GOF, respectively), higher flexibility, etc. [19].

The inherent higher sensitivity provided by the MMI technology compared to other OFS technologies, together with the interesting mechanical properties of POFs, makes them very promising for hydrostatic pressure applications, making the study of POF-MMIs very promising. Due to the advantageous properties of POFs, it is not surprising to find works reporting the use of POFs in sensor applications [20]. Technologies such as FBGs [13], [14], [21]–[23], LPGs [24] and MMIs [25], [26], have been commonly implemented with POFs, namely to improve the capabilities reported by GOF sensors. Specifically talking in hydrostatic pressure applications, technologies based on FBGs [22], [23] and LPGs [27], have already been reported. Despite that, the potential of POF based MMIs has not yet been explored in this field. Due to that, in this thesis it will be shown the results of the hydrostatic pressure characterization of a GOF-MMI and then, it will be compared with the results of a POF-MMI.

Along with MMIs, long period gratings (LPGs) are also another fiber optic sensor that has been subjected to a lot of research. This fiber device holds important features, such as the low-out-of-band losses in transmission signal, having a good signal-to-noise ratio, its versatility (it can be manufactured with different periods in order to tune the resonance wavelength), it's high sensitivity to several parameters, and the ability to be used in real time measurements. Due to these advantages, it is no surprise to find several applications of these devices , such as in gain flattening in erbium doped fiber amplifiers, gain equalizers [28], comb filters [29], mode converters [30], sensors [31], among others [32]. Regarding sensor applications, LPGs have been reported to measure several parameters, including: torsion [33], curvature [34], strain [35], temperature [36], humidity [37], among others [38]–[40].

Currently, there are two main types of LPGs, namely the ones that are permanently written in the fiber and the ones that are mechanically induced. To produce a permanent grating, it is possible to use various methods, such as radiation through CO_2 laser [41], UV laser [42], infrared femtosecond laser [43], ion beam [44], and electric arc discharge [45]. Regarding mechanically induced gratings, they can be induced by pressing a periodic grooved structure onto an optical fiber, such as 3D printed grooved plates [46], grooved plate [47], or using laminated plates [48]. Other means to induce LPGs have been reported through the application of strain to a corrugated optical fiber as is described in references [49], [50].

Among the mechanically induced LPGs, the most interesting ones are the ones based on corrugated structures, since they do not require additional parts to induce the grating. The

production of these LPGs has been described through two different methodologies: using photolithography methods followed by an etching process [51] or by deposition of a thin film of silver (Ag) by thermal evaporation followed by an etching process [52] or by deposition of a layer of SU-8 [53]. These three processes have something in common, which is the fact that all processes are extremely sophisticated and employ expensive equipment, along with the necessity of qualified personnel to work with that equipment. As a way to solve these problems and also to explore the advantages of these sensors, in the last part of this thesis it will be reported an easier and cost-effective technique to produce corrugated LPGs. This will be done through the periodical deposition of a photopolymerizable resin on a single mode fiber (SMF), followed by an etching process. The potentialities of the structure will be analyzed to external stimulus, such as strain, displacement and temperature. The capability to tune the wavelength of the resonance filter will be also shown by changing the period of the structure, making it a promising technology to act as a filter.

1.2. Structure of the thesis

In the first chapter of the thesis, it will be given the motivation behind this work. The strengths and weaknesses of the current state of art are mentioned and solutions are proposed in order to get better sensitivities with the desired sensors. The outline of the work is also given in this chapter.

On the second chapter it is explained the general theoretical principles and structure of optical fibers. A brief review of the different optical fiber sensors reported in literature is given. The working principles of the fiber structures explored in this thesis, namely multimodal interferometers and long period gratings will then be followed.

On chapter three, it will be explained the experimental procedures used to produce the desired multimodal interferometers, how the characterizations of these sensors were made, the involved simulation results and the results of the hydrostatic pressure characterizations.

Chapter four is dedicated to the experimental procedures used to produce the corrugated long period grating structures, the characterization of such structures to strain, displacement and temperature and their corresponding results as well as discussion.

In chapter five, the main conclusions of the work will be given, highlighting the main achievements undertaken in this thesis.

1.3. Contributions

- Part of this work, namely the one related to the MMI technology, served to write a journal paper, which was published on May 5th 2023 in the IEEE Sensors Journal, quoted in quartile 1 and with an impact factor of 4.7. The details of this paper journal are described below:
  "N. F. Valente, L. Bilro and R. Oliveira, "Hydrostatic pressure sensor based on polymer optical fiber multimode interferometer," IEEE Sensors Journal, DOI: 10.1109/JSEN.2023.3272172".
- The work developed in this thesis regarding the topic of mechanically induced LPGs has been driven from the 3rd year project, which resulted in the publication of the conference paper at the EOSAM conference in 2021. The details of that paper are described below:
  "N. F. Valente, L. Bilro, and R. Oliveira, "3D printing of long period gratings for curvature applications," vol. 255, 2021, doi: https://doi.org/10.1051/epjconf/202125512001."
- The work related to the LPG technology described in this thesis was submitted for presentation in the 28th International Conference on Optical Fiber Sensors (OFS28). This conference is the major conference in the optical fibers sensor community, and this year, it will be held in Hamamatsu in Japan, from 20 to 24 November 2023. The details of the paper are described below:
  "N. F. Valente, J. Preizal, L. Bilro, F. Figueira, R. Oliveira, "Corrugated long-period grating for strain, displacement and temperature sensor applications", 28th International Conference Optical Fiber Sensors 2023 (OFS), submitted on 19 May 2023.

2. Theoretical principles

2.1. Optical fibers

Optical fibers are cylindrical dielectric waveguides that usually consist of three layers: the core, that corresponds to the most inner region, the cladding that surrounds the core, and the coating, which is the most outer region, and used to as a reinforcement layer. A schematic representation of the cross section of a step-index (SI) optical fiber can be seen in Figure 1.

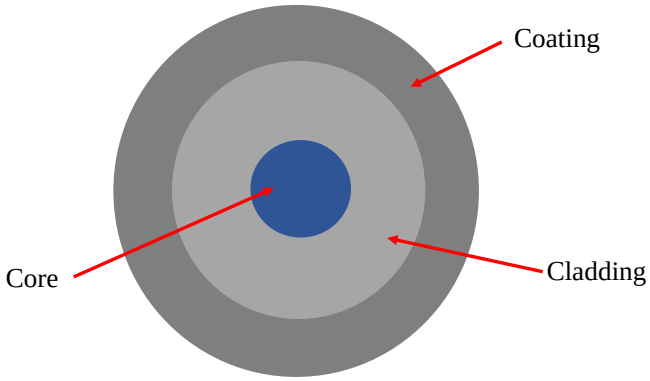

Figure 1. Schematic of the cross section of a SI optical fiber.

In an optical fiber, light propagates only in the core region due to total internal reflection (TIR), between the core and cladding regions [54]. This phenomenon is schematically shown in Figure 2.

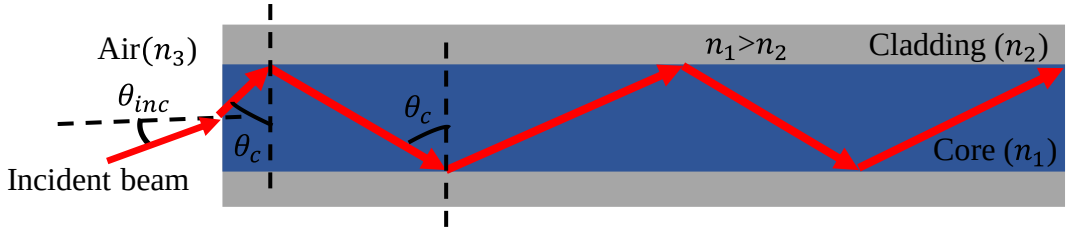

Figure 2. Schematic of the total internal reflection phenomenon in a SI optical fiber.

When a light ray propagates in a medium with a refractive index n_1, and this ray strikes with a certain angle (θ_1) in a surface of another medium with a different refractive index, n_2, part of it will be refracted with an angle θ_2, and the remaining will be reflected. The relation between the n_1, n_2, θ_1 and θ_2, can be explained by the Snell-Descartes law [55]:

$$n_1 \sin\theta_1 = n_2 \sin\theta_2 \quad (1)$$

In this equation, if $\theta_2 > 90^o$, then, the incident ray will be totally reflected. This angle is called critical angle (θ_C), and can be rewritten as:

$$\theta_c = sin^{-1}\frac{n_2}{n_1} \quad (2)$$

From equation (2), it is possible to verify that the refractive index of the second medium needs to be lower than the refractive index of the first medium, namely for the TIR to occur, being this exactly what happens in optical fibers, where the refractive index of the core is higher than the refractive index of the cladding.

Optical fibers can be grouped into two main categories, namely step-index and graded-index (GI) [55]. The difference between them relies on the refractive index distribution,

which describes a step-index profile for SI fibers and a graded index profile for GI fibers. Generally, SI fibers can be found in two main groups, namely single-mode fibers (SMFs) and multimode fibers (MMFs). An optical fiber is said SM if it only allows the propagation of only one mode, a mode in its simplest form corresponds to electric and magnetic field distribution transverse to the direction of light propagation in the waveguide. This occurs when the normalized frequency (*V*) is lower or equal to 2.405 [56], being *V*, given by the following equation:

$$V = k_0 a \sqrt{n_1^2 - n_2^2} \tag{3}$$

where k_0 is the wave number ($k_0 = \frac{2\pi}{\lambda}$, where λ is the vacuum wavelength), a is the radius of the fiber core, n_1 the refractive index of the core and n_2 the refractive index of the cladding. For MM fibers, they can propagate several modes, being an estimate of the number of modes given by: $M = \frac{V^2}{2}$.

In GI fibers, the core has a refractive index that is higher on the center and decreases until the outer edges. The variation of the refractive index of the core along the radial distance is normally achieved by doping the central core region with a higher refractive index material. The refractive index of the cladding is also lower than the refractive index of the core, however it is usually constant along the radial distance. In this type of fiber, the light follows a curved path, due to the graded index profile of the core refractive index, this allows to reduce problems associated to dispersion, which are problematic in fiber optic communications.

A representative scheme of the different fibers described above can be seen in Figure 3.

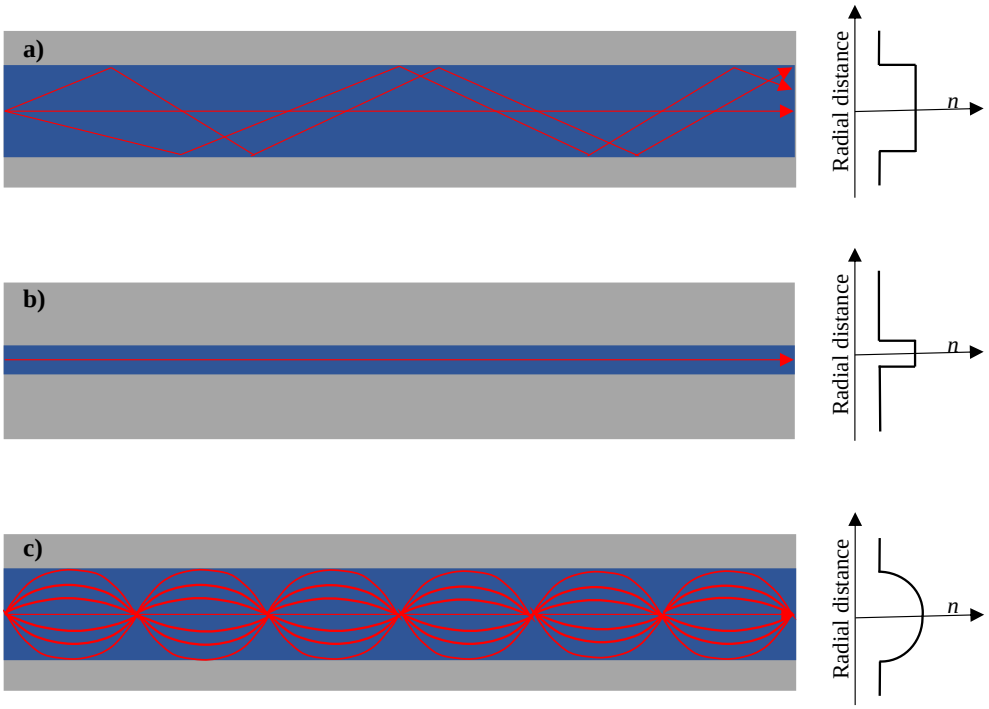

Figure 3. Refractive index profile of a), c) MM and b) SM optical fibers. The SI profile is seen in a) and b), while the GI profile is seen in c).

2.2. Optical fiber sensors

OFS have many advantages over the more traditional sensors, as is the case of electrical sensors. Some of those advantages are related to their multiplexing capabilities, the large bandwidth, the immunity to electromagnetic interference, their low losses, allowing to run long distances and reach remote or dangerous locations, and their ability to be used in harsh environments due to their toughness and resistance.

OFS can be grouped into two main types [57], namely, intrinsic or extrinsic. In an intrinsic sensor the optical fiber is the sensing element, while in an extrinsic sensor, the optical fiber serves only as a transparent medium used to propagate the light to the place where the measurement is being done, which is outside the fiber region. Intrinsic sensor types can be used to measure various properties, such as chemical [58], temperature [59], deformations [60], etc. The methodologies commonly used to produce these sensors are mostly fiber Bragg gratings [61], long period gratings [62], Fabry-Perot interferometers [63], multimode interferometers [64], among others. Among these techniques, the most cost effective and simpler sensors are the ones reported for LPGs and MMIs.

2.2.1. Multimodal fiber optic interferometers

Fiber optic MMIs are structures based on a MMF section fusion spliced between two SMFs. A representative scheme of this fiber structure is shown in Figure 4.

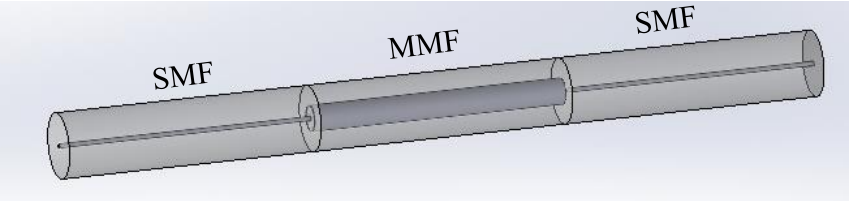

Figure 4. Representative scheme of an MMI composed of a MMF sandwiched between two SMFs.

When the fundamental mode of a SMF enters into the section of a MMF, it promotes the excitation of higher order modes and leads them to interfere along the MMF length. The accumulation of these interferences leads to the formation of replicas of the input field in amplitude and in phase, along the length of the MMF. The location where these replicas occur, also called self-images, can be determined at the length, *L*, using the following equation [65]:

$$L = N\frac{nD^2}{\lambda} \tag{4}$$

where *N* is the number of self-images, λ is the free space wavelength, and *n* and *D*, are the refractive index and the diameter of the MMF core, respectively. Considering the case where the MMF is cleaved at a distance in which one of the self-images is formed, the spectrum will appear with a well-defined peak power centered at λ. Equation (4), can be rewritten as $\lambda = N\,{nD^2}/{L}$, which shows that any change on *n*, *D* or *L*, can lead to a measurable shift in the peak power wavelength ($\Delta\lambda$). Because of this property, MMIs have been employed in a wide range of sensor applications [14], [16], [18], [66].

Considering the optical fiber as an isotropic material, the fractional wavelength change, $\Delta\lambda/\lambda$, induced in the MMI spectrum, can be written as [67]:

$$\frac{\Delta\lambda}{\lambda} = \left(\frac{1}{L}\frac{dL}{dP} + \frac{1}{n}\frac{dn}{dP}\right)\Delta P \tag{5}$$

where L is the length of the MMI, n is the effective refractive index of the core of the MMF and ΔP is the pressure change. The fractional length change and the fractional refractive index change are given by the following equations:

$$\frac{\Delta L}{L} = -\frac{(1-2v)P}{E} \tag{6}$$

$$\frac{\Delta n}{n} = \frac{Pn^2}{2E}(1-2v)(2p_{12}+p_{11}) \tag{7}$$

where E is the fiber Young's modulus, v is the Poisson ratio of the material, p_{11} and p_{12}, the strain-optic coefficients and P, is the applied pressure.

Equation (5) is well adapted to predict the response of a GOF-MMI. However, for POFs, this equation is no longer adequate. This occurs because during the POF production process, the polymer molecular chains tend to align along the length of the fiber, and, as a consequence, the properties perpendicular and parallel to the fiber axis are not the same. Annealing the fiber helps to reduce this effect, but the material will still show some residual stresses. Therefore, POFs cannot be considered isotropic and a more detailed equation needs to be described [22]:

$$\Delta\lambda = -\lambda\left(\frac{P}{E_t}(1-2v_t) - \frac{n^2P}{2}\left(\left(\frac{1}{E_p} - \frac{v_p}{E_p} - \frac{v_t}{E_t}\right)(p_{11}+p_{12}) + \frac{p_{13}}{\mathrm{E}_t}(1-2v_t)\right)\right) \tag{8}$$

being υ_t and υ_p the relevant Poisson's ratio, E_t and E_p, the Young's modulus parallel and perpendicular to the POF axis and p_{13} the component of the strain-optic tensor.

2.2.2. Long-period gratings

Among the existing optical fiber sensors, there is particular interest in those based on the grating technology. The reason is due to its easy reproducibility, its multiplexing capabilities, their low out-of-band loss, and its easiness in tuning the spectral location of the resonance band. Fiber gratings can be grouped in two main categories, namely, short-period gratings, also known as fiber Bragg gratings, and long-period gratings. The difference between them lies in their period, where for the former, is on the order of hundreds of nanometers, while for the latter, it is on the order of several tens of micrometers up to a millimeter [62]. In these periodic refractive index structures, the fundamental co-propagating core mode, can couple to the counter-propagating core mode as is the case of FBGs, and to the co-propagating cladding modes in the case of LPGs. For FBGs, the transmission spectrum presents a localized attenuation band for a wavelength that satisfies the Bragg condition. Regarding LPGs, the transmission spectrum will have specific

attenuation bands, each corresponding to coupling of the core mode to a specific cladding mode. The location where these resonance bands occur are described by the following expression [68]:

$$\lambda_i = (n_e - n_i) * \Lambda \tag{9}$$

where n_e is the effective refractive index of the core mode, n_i the effective refractive index of the i^{th} cladding mode, and Λ is the period of the refractive index modulation, or in other words the period of the grating. A representative scheme of the working principle of an LPG can be seen in Figure 5.

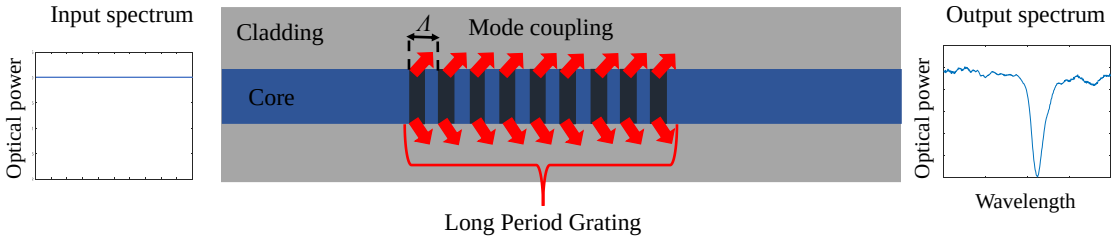

Figure 5. Working principle of an LPG. The core mode couples to the cladding mode generating a spectral dip loss in the transmission spectrum.

A broadband source is injected into the core of the fiber, reaches the grating and exits the fiber. The output spectrum presents an attenuation band corresponding to the core to cladding mode coupling. From equation (9), it is possible to observe that the spectral location of the attenuation bands depends on the effective refractive index of the core and cladding modes and the period of the grating. Therefore, any change in the external environment (e.g.: temperature, deformation, refractive index, etc.) will lead to a change in these parameters and consequently to the spectral location of the attenuation band.

Considering the particular case where an LPG is subjected to an external load, as is the case of strain, it is possible to estimate the modulation of the refractive index suffered in the fiber core through the strain-optic effect, as is detailed in the following expression [69]:

$$\Delta n = -n_1 p_e \varepsilon = -n_0 p_e \frac{F}{EA} \tag{10}$$

where n_1 is the refractive index of the core, p_e is the photoelastic constant, ε is the deformation, F the applied force, E the Young modulus, and A the area of the transversal section of the fiber. From equation (10), it can be concluded that the modulation of the refractive index will be inversely proportional to the Young's modulus and the cross-sectional area of the fiber, and directly proportional to the applied force and this is special relevant for LPGs produced through corrugated structures. In a corrugated LPG, the distribution of the stress along the fiber is not homogeneously distributed, since the fiber diameter is modulated along the fiber axis, thus, when longitudinal strain is applied to this fiber structure, the strain distribution will be also modulated. This will cause a refractive index modulation along the length of the structure due to the strain-optic effect, leading to the creation of an induced LPG. This structure will have the capacity to couple the fundamental core mode with a co-propagating cladding mode traveling in the cladding region, causing the appearance of resonance bands in a transmission spectrum as it happens

with a regular permanent LPG. However, the amount of strain acting on this structure allows to modulate the coupling strength and thus the attenuation of the resonance band.

Considering now the case where a corrugated structure is subjected to a bent condition, the refractive index modulation will occur through a different mechanism. In this case, the inner side of the fiber under a bent condition will be under a compressive stress while the outer fiber region to a tensile stress This allows to modulate the refractive index of the inner and outer parts differently. For the sake of better understanding of the phenomenon, it is shown in Figure 6, a representative scheme of the refractive index changes that occur in an optical fiber when subjected to a bent condition.

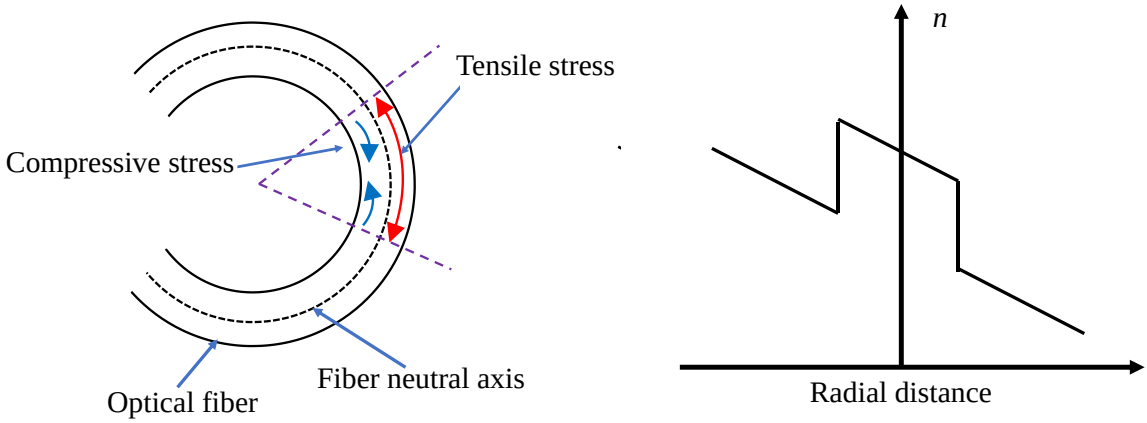

Figure 6. On the left side it is shown the stress acting in the inner and outer most region of an optical fiber, when subjecting it to a bent condition. On the right side it is shown the corresponding effect on the refractive index of the fiber along the radial distance.

So, when an optical fiber is in a bent condition, the refractive index modulation can be written through the following equation [70]:

$$n(x,R) = \left(1 + \frac{x}{R_{eff}}\right) n(x) = \left(1 + \frac{x}{1.280R}\right) n(x) \tag{11}$$

being x the radial coordinate on the waveguide, R_{eff} the effective bend radius and R is the bending radius. From this equation, it can be concluded that the inner part of the fiber will have a higher refractive index than the outer due again to the strain-optic effect.

Without a bending being applied to the LPG, the transmittance of it can be explained by the following relationship, [68]:

$$T = cos^2(k_{co-cl}^{ac} l) \tag{12}$$

where l is the length of the grating and k_{co-cl}^{ac} is the *ac* component of the coupling coefficient between the core mode and the cladding mode involved.

3. Multimode interferometers

3.1. Production of multimode interferometers

To produce the optical fiber MMI sensors, it was used two types of MMFs, namely a GOF, reference: AFS50-125Y, from Fiberguide Industries, Inc., and a polymethylmethacrylate (PMMA) POF, reference: MMPOF 01, from Paradigm Optics, Inc. These MMFs were spliced (i.e. through hot and cold splices), between two standard SMFs, ITU G.652, distributed by Cabelte S.A.

The multimode GOF has a SI profile, having a core and cladding diameters of 50 µm and 125 µm, respectively. It is composed of a pure silica core with n(@1.55 µm) ~1.444, and a fluorine doped silica cladding with n(@1.55 µm) ~ 1.424. Regarding the POF, it has a SI profile with core and cladding diameters of 240 µm and 250 µm, respectively. The core material is made of PMMA, having refractive index of n(@1.55 µm) ~1.480, while the cladding is a fluorinated polymer material with a slightly lower refractive index. A common practice when using POFs is to anneal them in order to partially release the frozen stress left during the drawing process. Thus, the POF used in this work was annealed at 90 ºC for one hour.

Since the POF has an outer diameter much larger than that of the SMF (~250 µm vs. 125 µm), this would result in difficulties to align them during the splicing process. Because of that, the POF was etched in acetone to reach a similar diameter as that of the SMF. To know the necessary time, several POF terminals were immersed at the same time in acetone. Then, at every five minutes, each fiber terminal was removed from the solution, and its diameter was measured. A calibration curve was then performed as it is shown in Figure 7.

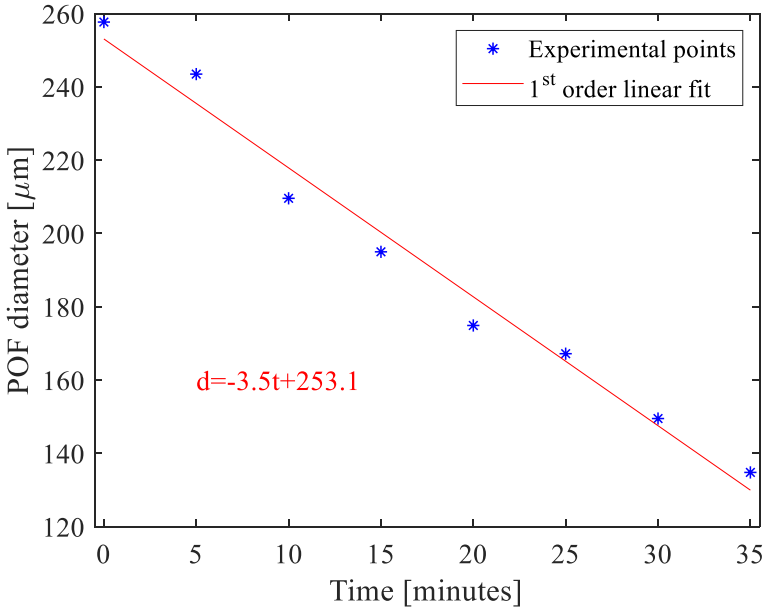

Figure 7. Diameter evolution of a PMMA based POF immersed in acetone.

From the figure above, it is possible to see that the etching rate was ~3.5 µm/minute. Thus, to reach a final diameter of ~125 µm it was necessary an etching period of ~36 minutes. The diameter obtained after the etching process was 127 µm.

On what concerns the SMF, it is composed of a pure silica cladding and a germanium doped core, being the refractive index close to 1.444 and 1.450, and the diameter equal to 8.1 and 125.0 µm, respectively.

The number of self-images used to produce the GOF-MMI and POF-MMI, were equal to 8 and 2, respectively. As known from literature [71], N is inversely proportional to the linewidth of the peak power that appears at λ. Since D(POF) = 127 µm > D(GOF) = 50 µm, a lower number of images is required for the MMI based POF compared to that of the GOF. This occurs because a higher number of modes are allowed to propagate in the multimode POF. Considering n and D values described above for the POF and GOF and considering that the peak power is desired to be at the near infrared region, the MMF lengths obtained from (4) were 19.0 mm and 30.8 mm, for the GOF and POF, respectively. This corresponds to obtain peak power wavelengths cantered at 1520 and 1550 nm, respectively.

To cleave the multimode glass optical fibers (MM-GOF) with the desired length, it was used a 0.1 µm resolution motorized linear stage (MFA-CC, from Newport ®). This was used to precisely position the fiber against the diamond blade of the fiber cleaver, model CT30 from Fujikura Ltd. To cleave the MM-POFs a similar setup was used, however, the commercial fiber cleaver was replaced by a homemade blade rotation system. The exemplificative setups used to cleave the GOF and POF are shown in Figure 8 a) and b), respectively.

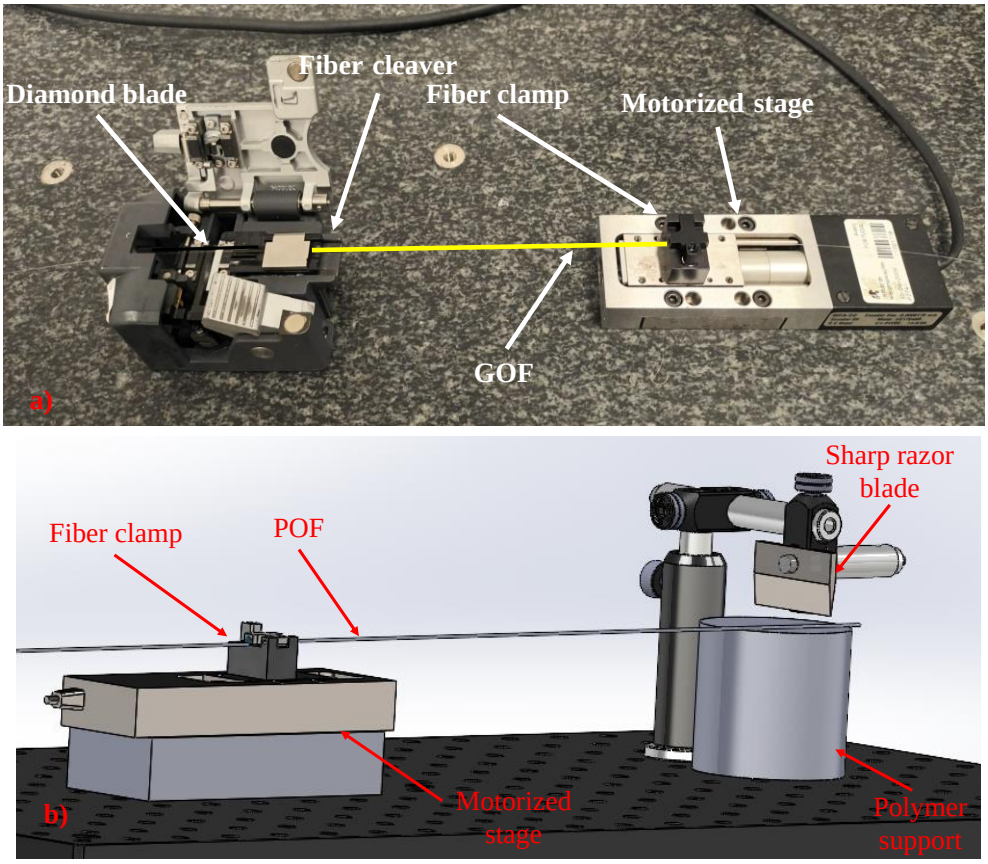

Figure 8. Experimental setup used to cleave a) GOFs and b) POFs, with precise lengths.

Following the cleaving process, each of the terminals of the MMFs, were fusion spliced to standard SMFs. For the MM-GOF, the standard hot-fusion splicing process was used, namely through a Fujikura FSM-60S machine, sold from Fujikura Ltd. Regarding the MM-POF a cold-fusion process was done. This was made manually in a dedicated setup. This was composed of a 3-axis micrometer stage (MBT616D from Thorlabs®), used to align the terminals of the POF and GOF, two orthogonal cameras coupled to telecentric lens (2X magnification) to help the alignment, and an objective magnification lens (40 X) used to collimate the beam and project it onto a laser beam profiler (LBP), BeamOn IR1550, from Duma Optronics Ltd. The experimental assembly used for the cold-fusion process is shown in Figure 9.

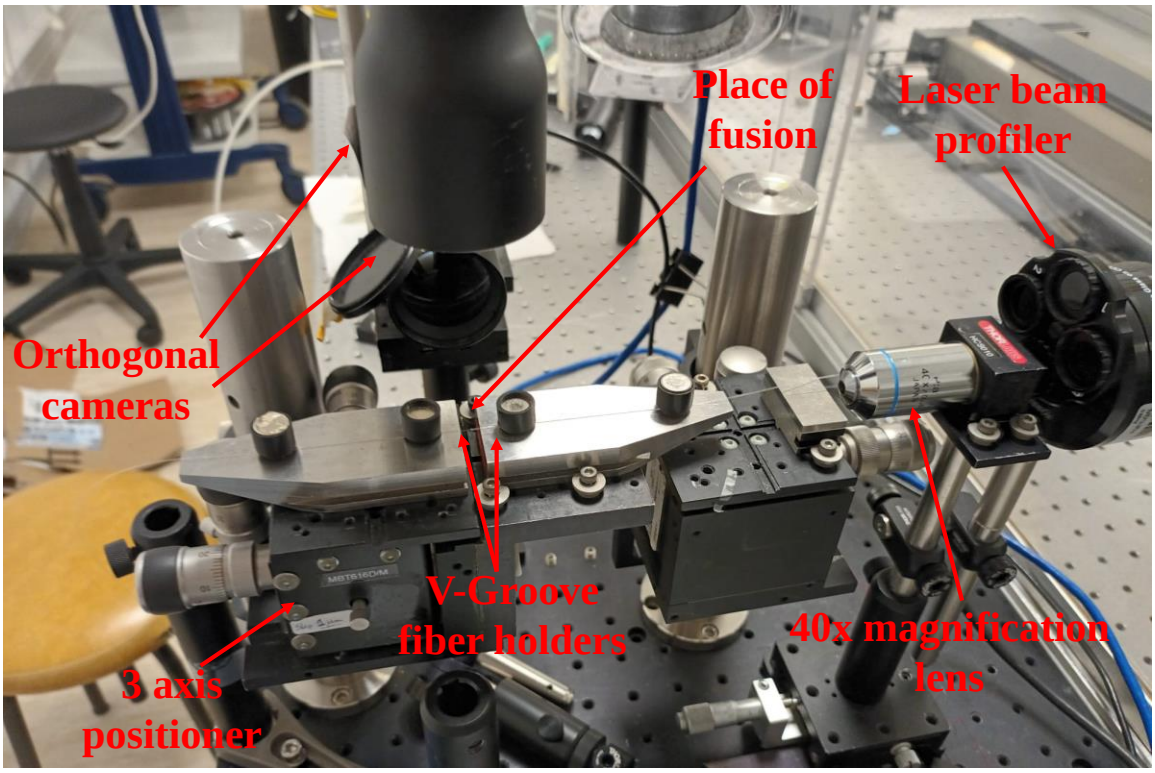

Figure 9. Experimental setup used to fuse the GOF and POF through the cold-splicing process using a UV photopolymerizable resin.

The first alignment of the fiber terminals was made in real time through the cameras, this was a cladding alignment and did not allow precise alignment. Then light was injected in the SMF and the near-field image at the output terminal of the POF was visualized in real time in the LBP. This allowed to observe the modes propagating into the POF and thus, fine adjustments were done to obtain the best optical fiber power distribution, which was an indicative of the proper transversal fiber alignment. After this procedure, the fiber terminals were bonded together with a UV photopolymerizable resin, NOA 86H, from Norland Products Inc. The resin was applied to the POF and GOF terminal contact region, through the help of an external SMF covered with resin on its tip. This UV resin has a tensile strength similar to that of the POF, allowing to make a robust connection between the fibers. Furthermore, several layers of resin were added to the region to enhance its strength. Each

layer of resin was photopolymerized by a UV gun (Opticure LED200, from Norland Products Inc.), having 365 nm operational wavelength and an irradiance of 2.5 W/cm^2. The polymerization period was set to approximately 15 seconds.

3.2. Characterization to hydrostatic pressure

In order to carry out the hydrostatic pressure tests, the MMI sensors were inserted in a pressure pump (model P18, from Enerpac(r)) filled with mineral oil. Care was taken to insert the MMIs in a straight configuration, avoiding possible curvature artifacts that could cause erroneous measurements.

Tests were carried out by applying pressure in steps of 10 bars and waiting 10 seconds before spectra acquisition. It was necessary to wait this time to acquire the spectra in order to let the polymeric chains of MMI-POF stabilize after each pressure application. The pressure measurements were taken with a pressure gauge with resolution of 1 bar. Due to the confined space of the pressure vessel, the characterization of the GOF-MMI and POF-MMI was done separately. To acquire the spectral response of the sensors during the pressure characterizations, it was used an optical fiber interrogator (Hyperion Si155, from Luna Innovations Inc.). The measurements were made in transmission using two of the available In/Out interrogator ports. A representative scheme of the experimental setup can be seen in Figure 10.

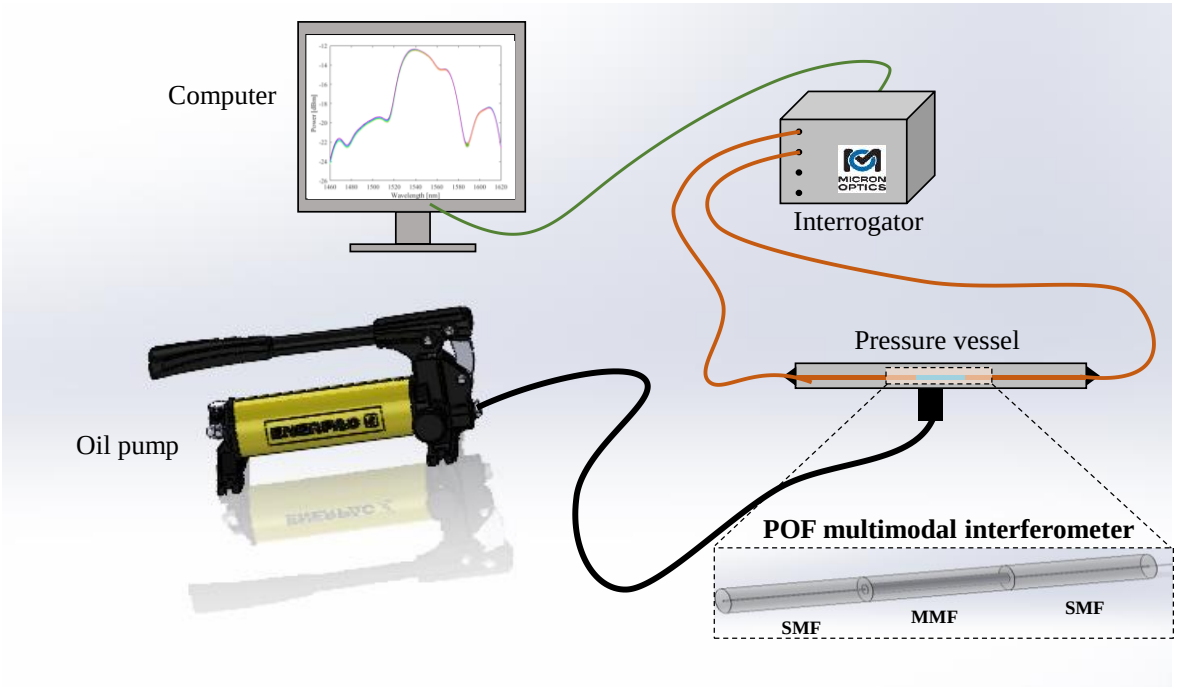

Figure 10. Representative scheme of the experimental setup used to do the hydrostatic pressure characterizations tests.

3.3. Numerical modelling

To predict the spectral response of the GOF and POF multimode interferometers when subjected to hydrostatic pressure, simulations have been performed to estimate the influence of the length change of the MMI, and also, the influence of the external refractive index change on the spectral response of the MMIs.

3.3.1. Glass optical fiber simulations

To estimate the influence of the hydrostatic pressure on the length change of the GOF-MMI, a simulation has been carried on the solid mechanics module of the SOLIDWORKS® software. The simulation considered a cylinder with a diameter of 125 µm and length of 19.0 mm (similar to the one used for the experimental part). The material was chosen from the simulator library to be glass. This has a Young's modulus of 69 GPa and a Poisson's ratio of 0.23. Next, one of the fiber terminals was fixed in the three dimensions, while the other was fixed only in the Z and Y directions and allowed to move along the fiber longitudinal axis (X direction). Lastly, to simulate the hydrostatic pressure, a force with 10 bars was applied radially to the fiber as is shown in Figure 11.

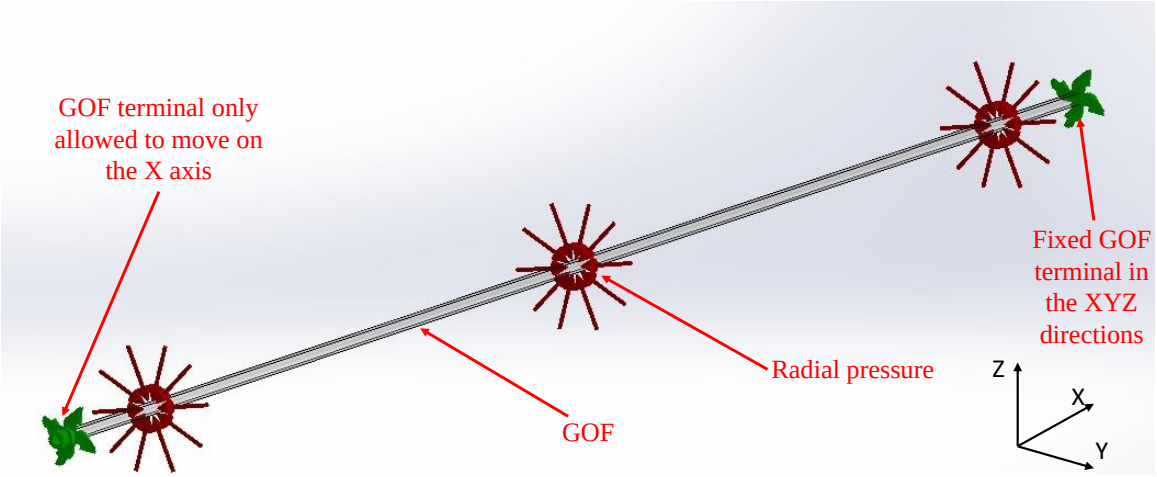

Figure 11. Image taken from the simulation showing the sketch drawn necessary to understand the elongation suffered by the GOF, when subjected to hydrostatic pressure.

After running the simulation, a positive displacement of 0.12 µm was obtained meaning that the fiber elongated whit positive hydrostatic pressure. This value was then fed into another simulation software, namely in the waveguide optics design software, from OptiBPM, registered from Optiwave Systems Inc. The simulation is based on the beam propagation method and was used to calculate the output optical power for a range of wavelengths, allowing to reconstruct the spectrum of the MMI. This simulation was done for the original GOF length, and for the GOF with an additional length of 0.12 µm, allowing to check the differences between the unload and load cases. It was considered a diameter of 50 µm and 125 µm for the core and the cladding of the MMF, respectively. The refractive index of the core was defined as 1.444, and 1.424 for the core and cladding, respectively. Regarding the SMF, which is used to inject light at the left side of the MMF, it was used a refractive index of 1.450, and 1.444, and a diameter of 8.1 µm and 125 µm, for the core and

cladding, respectively. The length of the SMF was 0.2 mm. Also, the simulation considered an external layer, used to mimic the surrounding refractive index, defined as n_{ext} = 1.000 for the case when the MMIs are in air and n_{ext} = 1.450 when the MMIs are inside the pressure vessel filled with the oil. The simulation was made for the wavelength region between 1500 nm and 1600 nm, with a resolution of 1 nm. An example of the electric field amplitude distribution along the length of a GOF-MMI with length of 19.0 mm and surrounded by n_{ext} = 1.000 is present in Figure 12.

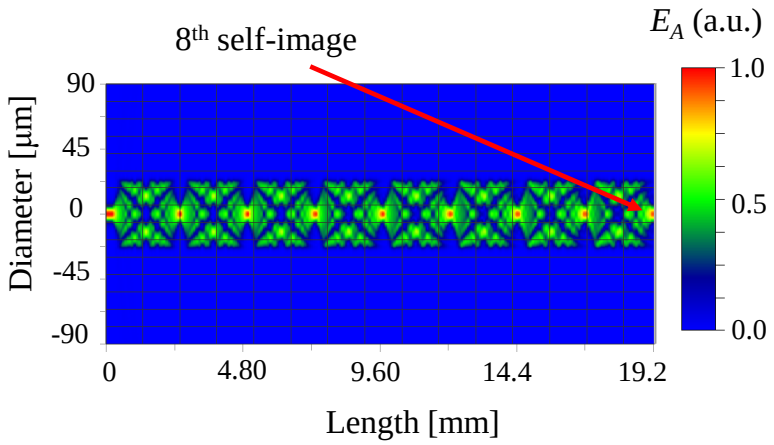

Figure 12. Normalized electric field amplitude distribution (E_A) along the whole length of a GOF-MMI, obtained when the external medium is air and λ = 1520 nm.

As expected, the figure above presents eight self-images as predicted in section 3.1. By measuring the optical power at the end of the MMF and in its central region, and doing this for each wavelength, it was possible to obtain the theoretical spectral power distribution, for the case when the MMI is with and without a 10 bar hydrostatic pressure. The results are shown in Figure 13.

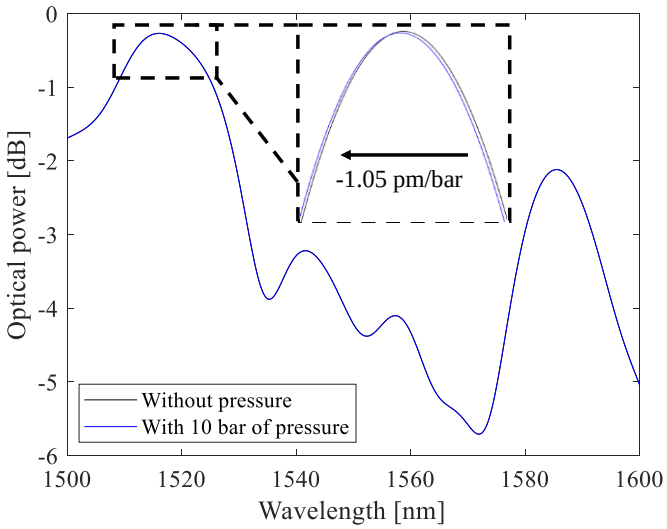

Figure 13. Theoretical spectra of the GOF-MMI when the interferometer is with and without a 10 bar hydrostatic pressure.

From Figure 13, it can be seen that the peak power of the GOF-MMI appeared at the 1520 nm wavelength region as predicted in section 3.1. Also, it can be observed that when the GOF-MMI is under hydrostatic pressure, the spectrum is blue-wavelength shifted (i.e. -

1.05 pm/bar). One important thing to notice is that the core of the GOF-MMF is not exposed to the external environment, thus, the refractive index changes of the oil under pressure, do not affect the output spectra.

3.3.2. Polymer optical fiber simulations

For the POF-MMI it was not possible to determine the theoretical length change when the fiber is subjected to hydrostatic pressure. This occurred because PMMA is an anisotropic material and thus, a variety of parameters (see equation (8)) is required as input for the simulation software. Due to the absence of these parameters in literature, it was not possible to run this simulation. However, since the core of the PMMA fiber is exposed to the external environment, because of the etching process, and considering that the oil refractive index changes with pressure, it was decided to run a simulation to predict the theoretical spectral response of the interferometer.

For the simulation, the POF was drawn with a diameter of 125.0 μm and the refractive index was set to 1.480. The POF length was the one described on the experimental part (30.8 mm). The SMF was drawn with diameters of 8.1 μm and 125.0 μm, for core and cladding, respectively, and their refractive indices were set to 1.450 and 1.444, respectively. The length of the SMF was defined as 0.2 mm. The simulation was made for three different external refractive index media, namely n_{ext} = 1.00000, n_{ext} = 1.45000 and n_{ext} = 1.45002, corresponding to air, oil without hydrostatic pressure, and oil with a 10 bar hydrostatic pressure, respectively. The refractive index change of the mineral oil for the 10 bar pressure was estimated through the data presented in reference [72].

The electric field amplitude distribution along the length of the POF-MMI, obtained for the 1550 nm wavelength can be seen in Figure 14.

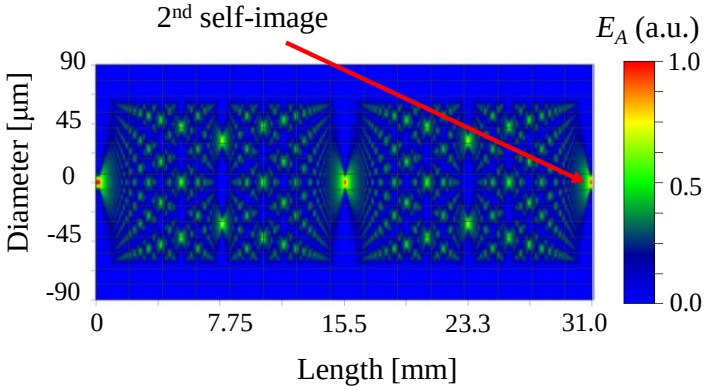

Figure 14. Normalized electric field amplitude distribution (E_A) along the whole length of the POF-MMI when the surrounding external layer was air and λ = 1550 nm.

As predicted from section 3.1, the POF presents two self-images at the wavelength of 1550 nm. After running the simulation for the wavelengths between 1500 nm and 1600 nm with steps of 1 nm and by determining the output power at the central region of the far end of the POF, it was possible to obtain the spectra of the POF-MMI for the three external refractive indices mentioned earlier. The results are shown in Figure 15.

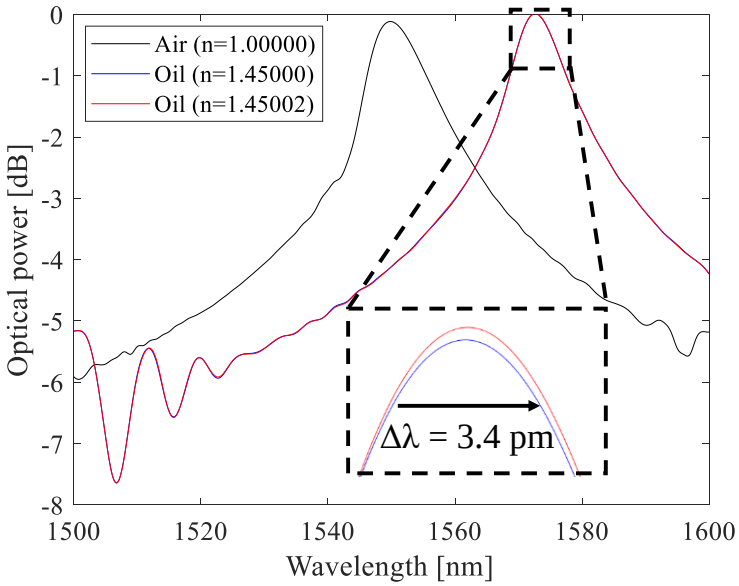

Figure 15. Theoretical spectra of the POF-MMI calculated for three different external media.

As shown from the figure above, when the external medium is air, the central peak appears at the 1550 nm wavelength as predicted from equation (4). When the external medium changes to the mineral oil (n_{ext} = 1.45000, without hydrostatic pressure), there was a red-wavelength shift of approximately 22 nm. Finally, when the refractive index of the oil increases to n_{ext} = 1.45002, as a consequence of the 10 bar hydrostatic pressure, a 3.4 pm red-wavelength shift is observed.

3.4. Responses of MMIs to hydrostatic pressure - experimental results

3.4.1. GOF-MMI results

Following the experimental procedure explained in section 3.2, it was obtained the graph of the optical power as function of wavelength for the hydrostatic pressure characterization for the GOF-MMI. The graph is shown on Figure 16.

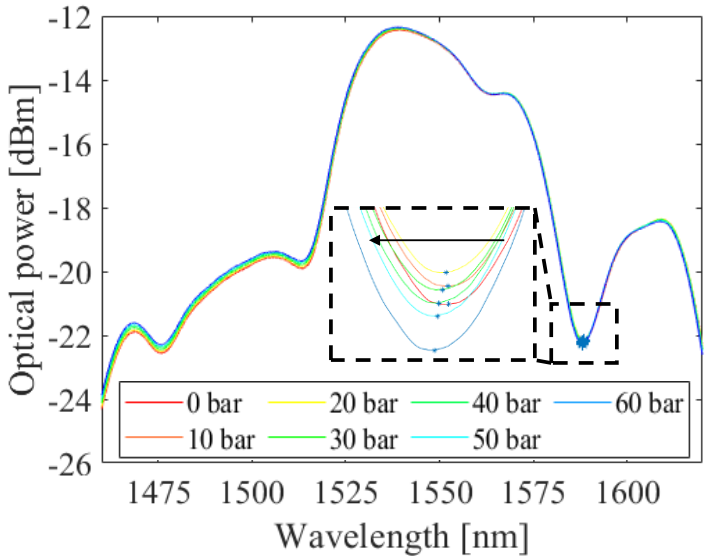

Figure 16. Transmission spectra of the GOF-MMI obtained for pressure changes between 0 bar and 60 bar in steps of 10 bar.

From Figure 16, it can be seen that the spectra are blue shifted with increasing hydrostatic pressure. By taking the dip power for the wavelength found at 1589 nm, it is possible to determine the hydrostatic pressure sensitivity of the sensor and consequently compare its value with the one obtained from the theoretical simulation. The dip was chosen instead of the peak power because of its narrower response, allowing to reduce the errors in determining the spectral wavelength shift. The experimental data points together with the linear fits can be seen on Figure 17.

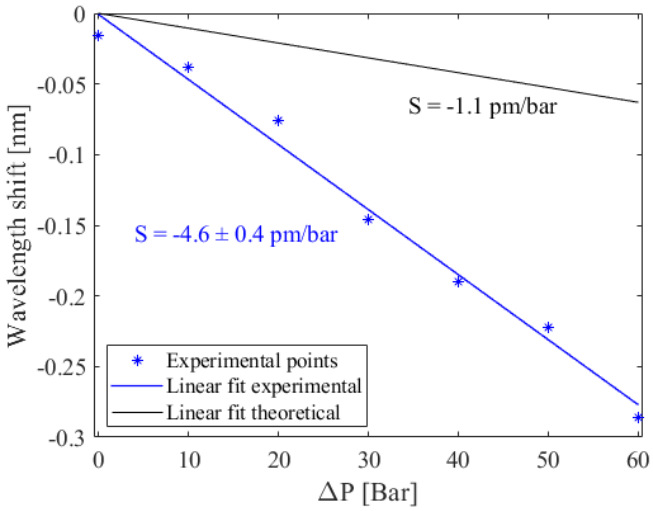

Figure 17. Wavelength shift as function of the hydrostatic pressure changes, obtained from the experimental and theoretical results for the GOF-MMI sensor.

As is seen from Figure 17, the wavelength shifts observed for each of the interferometers follow a linear response with the increase of the hydrostatic pressure changes. By applying first order linear fits to the experimental data points, it was possible to obtain sensitivities of -4.6 ± 0.3 pm/bar for the GOF-MMI. The sensitivity reported for this interferometer is identical to the one reported in reference [18] i.e. −2.4 pm/bar. The difference between the sensitivities could be explained by the different MMFs used to produce the MMIs.

The experimental results present a sensitivity almost four times higher than the one reached in the numerical modelling. A possible reason for this discrepancy could be due to the fact that in the simulation it was only considered the change in length of the fiber and not the refractive index change, the elongation of the fiber in the simulation, will cause a deviation in the wavelength where the peak power of the MMI will appear, by looking to equation (4), it can be concluded that if the length of the fiber is higher, the wavelength where the peak appears is lower, causing the blue shift observed both in the simulation and the experimental results, other factor that could have influenced the results could be the parameters used in the simulations which could not be exactly the same for the fibers used, since they were estimates taken from literature. To compare the numerical result with the analytical one reported in equation (5), it was used the parameter values used on the numerical analysis, namely $\upsilon = 0.23$ and $E = 69$ GPa, being also used the values of $p_{11} = 0.121$ and $p_{12} = 0.27$ from standard optical fibers. From this analytical calculation, it was obtained a theoretical value of −0.4 pm/bar. This value was close to the one reached in the numerical modelling, but eleven times lower that the one reached in the experimental results. The explanation for all these discrepancies can only be attributed to the theoretical values used in both numerical and analytical results, which do not match the real values of the fibers under study.

3.4.2. POF-MMI results

Following the experimental procedure explained in section 3.2 it was obtained the graph of the power vs. wavelength for the hydrostatic pressure characterization for the POF-MMI. The graph is shown in Figure 18.

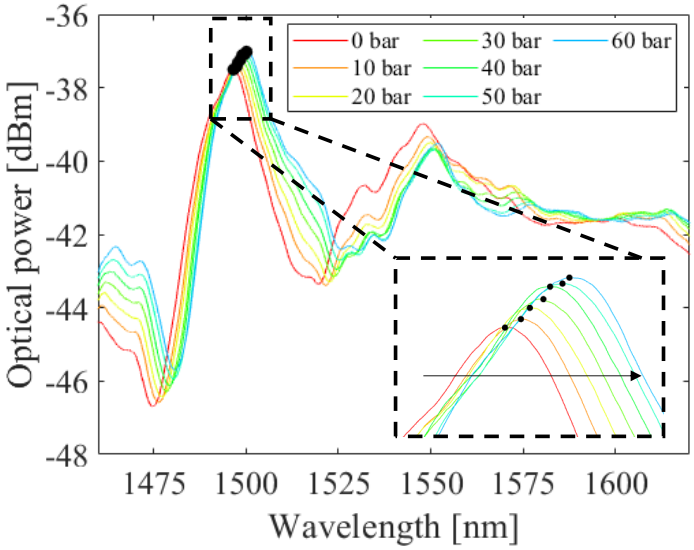

Figure 18. Transmission spectra of the POF-MMI obtained for pressure changes between 0 bar and 60 bar in steps of 10 bar.

From the graph shown above, it can be seen that the spectra were red shifted with the increase of pressure. By taking the peak power wavelength at ~1500 nm it was possible to estimate the hydrostatic pressure sensitivity response of the sensor. In Figure 19 it is shown the absolute values of the wavelength shift vs. hydrostatic pressure, for the POF-MMI sensor. For comparison purposes, it is also included the results of the GOF-MMI sensor.

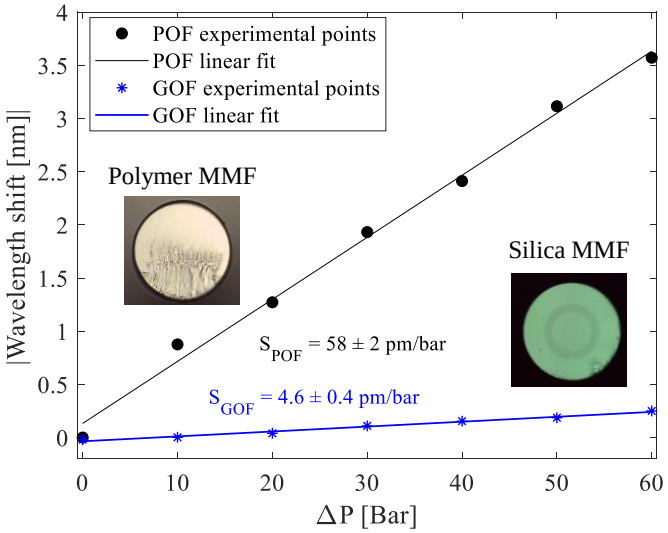

Figure 19. Absolute value of the wavelength shift vs. hydrostatic pressure changes for the POF and GOF based MMIs.

The wavelength shift observed for the POF-MMI and GOF-MMI presents a linear response for the whole characterization range. The POF-MMI presents a sensitivity of

58 ± 3 pm/bar, which is more than twelve times higher than the sensitivity obtained for the GOF-MMI. Also, the value achieved in this work was almost five times higher than the one reached for Bragg gratings written in POFs [22]. The positive wavelength shift response observed for the POF-MMI was in accordance with what is already reported in literature for Bragg gratings in POFs. This positive wavelength shift means that the contribution of the fractional length change is higher than the contribution of the fractional refractive index change. It is important to notice that the core POF interacts directly with the external environment, and changes on the external refractive index can lead to measurement errors. According to the simulations, it is predicted a wavelength shift of 3.4 pm for each 10 bar pressure changes. Based on this result, it expected a measurement error of about 0.34/58 = 0.6%/bar.

In order to compare the resolution of the sensors GOF- and POF-MMI sensors produced in this work, it can be considered a standard interrogation system with resolution of 5 pm. For such scenario, this will induce a resolution of ~0.1 bar and 1.1 bar for the POF-MMI and GOF-MMI, respectively, showing that a POF-MMI is more adequate to hydrostatic pressure sensor applications.

4. Corrugated long-period gratings

4.1. Experimental methods

4.1.1. Printing of the comb-like structure

In order to produce the corrugated long period gratings, it was necessary to draw a comb-like structure that allows the periodic deposition of a small amount of UV liquid resin along the length of the fiber. The first step consisted in designing the part in a computer aided designer (CAD) software. This was done through an available licence of SOLIWORKS®. The support of the structure consisted of a parallelepiped of 107 mm length, 2.5 mm width and 3.5 mm height. On top of it, a periodic set of cylinders were drawn with a diameter of 0.2 mm and height of 3.5 mm. Those will be used to transfer the resin from them onto the surface of the fiber. The period of the structure was reached through a trial-and-error approach, by printing the structure with periods ranging from 600 up to 1200 µm and checking if the resin was clogged between the set of cylinders. After this test, it was found that the necessary period was above 1060 µm. This period is a function of the surface tension of the resin onto the 3D printed part, and thus, different values could be reached depending on the materials used. The comb was designed to have 100 periods, giving a total length of 10.6 mm. It was chosen this high number of periods because it is known from the literature that narrower resonances are achieved for higher number of grating periods [42]. The representative scheme of the designed comb-like structure can be seen on Figure 20.

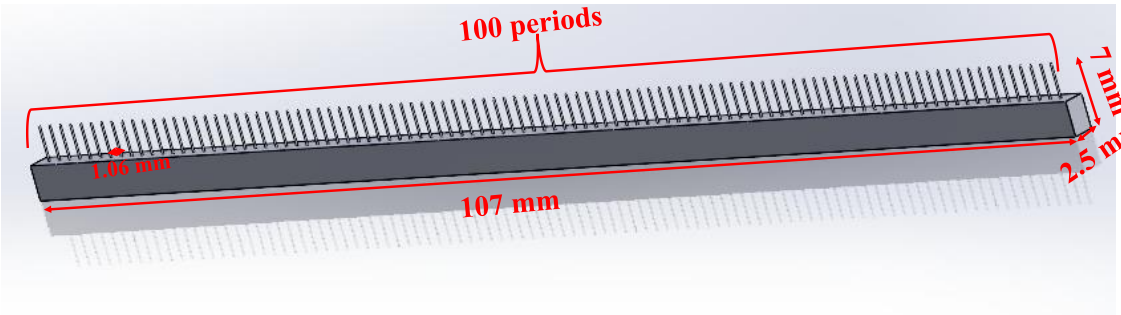

Figure 20. Representative scheme of the comb-like structure.

After designing the comb-like structure, the CAD file was exported to the slicer software of the 3D printer (Photon Mono SE from Anycubic®), who generates the file with the instructions for the printer. The 3D printer used for this process was a low-cost digital light processing (DLP) 3D printer that uses UV light (λ = 405 nm) to photopolymerize the liquid resin. This printer has an associated uncertainty of 47 µm, given by the pixel size of the printer. Furthermore, it can print layers with resolutions up to 1 µm. The structure was printed with a standard resin from Anycubic®, and the printing parameters were 50 µm for the layer thickness and with an exposure time of 10 seconds per layer. To firmly attach the structure to the printer build plate, it was used 6 bottom layers with an exposure time of 40 seconds. After the printing process, the structures were washed manually in a recipient full of isopropyl alcohol for a period of two minutes. This was done to remove the excess of resin that could be leftover on the structure. The result of the 3D printed comb like-structure can be seen on Figure 21.

Figure 21. 3D printed comb-like structure after the hardening and washing process.

4.1.2. Production of the corrugated fiber structure

To produce the corrugated fiber structure, an experimental setup was built as is shown in Figure 22.

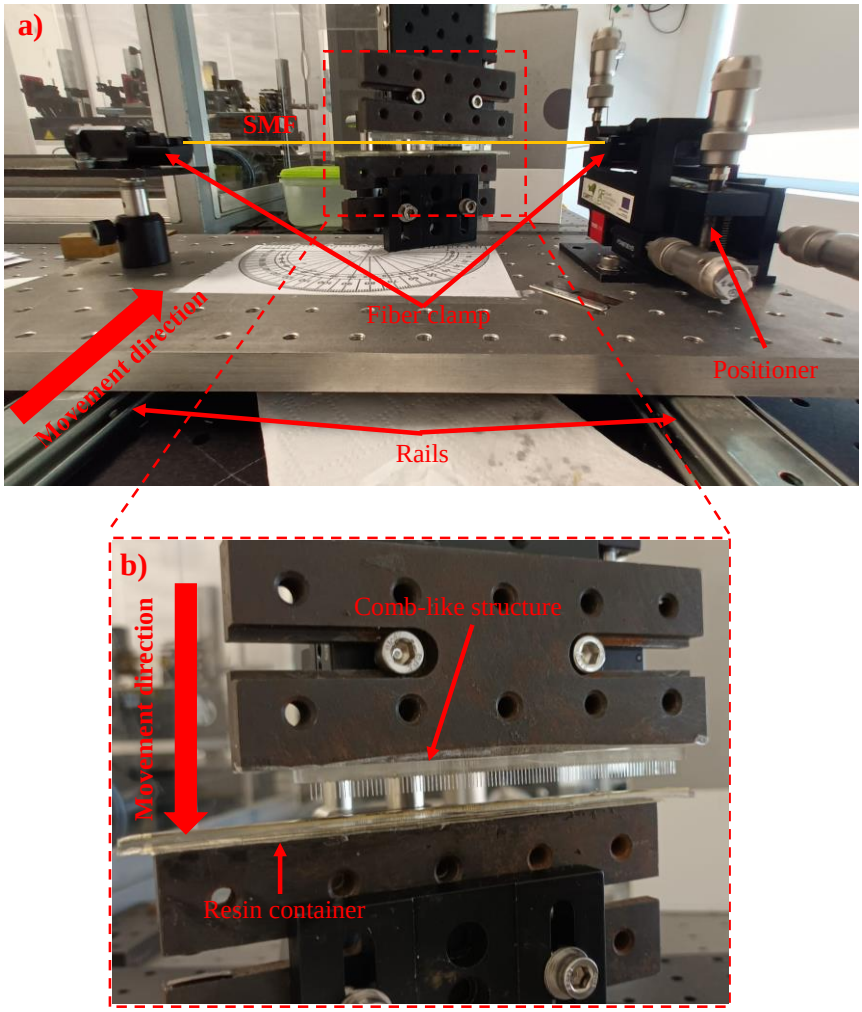

Figure 22. a) Experimental setup used to periodically deposit liquid resin on top of the SMF. b) Inset of the comb-like structure above the photopolymerizable resin container.

The setup shown in Figure 22 was based on a platform used to move the optical fiber (with the help of two rails), against the 3D-printed comb-like structure fixed onto a static arm. The optical fiber was a SMF, ITU G.652, distributed by Cabelte SA., and was stripped and secured on its terminals by two rotational fiber clamps. The distance between the clamps was higher than that of the length of the 3D-printed comb structure. The levelling process was done at one of the fiber terminals through a multiaxis positioner. In front of the platform that contains the fiber, the 3D-printed comb-like structure was mounted on a second platform able to move vertically. The comb-like structure was facing down and was parallel related

to the fiber. A resin container also 3D printed, was used to immerse the comb-like structure into the liquid resin. This is found right below the comb structure and can be easily accessed by the com structure through vertical movement of the platform. To leave a periodic pattern of liquid resin on the surface of the optical fiber, the platform containing the fiber was moved horizontally in the direction of the comb structure that was previously immersed in the liquid resin (i.e. standard resin used for the 3D printing). As the fiber passes through the comb structure, a small portion of the liquid resin found in each period of the comb-like structure was left on the surface of the fiber because of the surface tension. After this process, the periodic liquid resin pattern left onto the optical fiber was hardened using a handheld UV gun (Opticure LED200, Norland Products Inc.), having 365 nm wavelength and with an irradiance of 2.5 W/cm^2, for a period of thirty seconds. Then, the fiber clamps were rotated 180º to expose the opposite surface of the fiber, and later, the process was repeated. The period of the resin drops left on the surface of the optical fiber was easily controlled through the horizontal rotation of the comb-like structure related to the optical fiber, allowing the fiber to move through the comb structure with an angle, α, such that:

$$\Lambda_{\text{theo}} = \Lambda_{\text{comb}} \cos(\alpha) \tag{13}$$

where Λ_{comb} is the period of the comb and α is the angle that the comb structure makes with the optical fiber fixed between the fiber clamps. The results of the calculations can be seen in Table 1.

Table 1.Calculated theoretical periods as function of the tilt angle between the fiber and the comb-like structure.

Angle (α)	**Theoretical period (Λ_{theo})**
37.0º	850 μm
41.0º	800 μm
45.0º	750 μm
48.7º	700 μm

It was experimentally observed that for periods below 700 μm, the resin left by the comb onto the fiber joined because of the small distance between the resin drops. Liquid resins with a higher surface tension could be used, however, despite the use of different resins available on the laboratory, similar conclusive results were attained. The next step required to produce the corrugated LPG was the corrosion of the unexposed regions of the optical fiber. To this end, it was used hydrofluoric acid (HF) at 48%, from Fisher Scientific. To know the rate of corrosion, six SMFs were immersed in HF and each one was removed at every three minutes. The diameter of each sample was measured, and the calibration curve was obtained. The results can be seen on Figure 23.

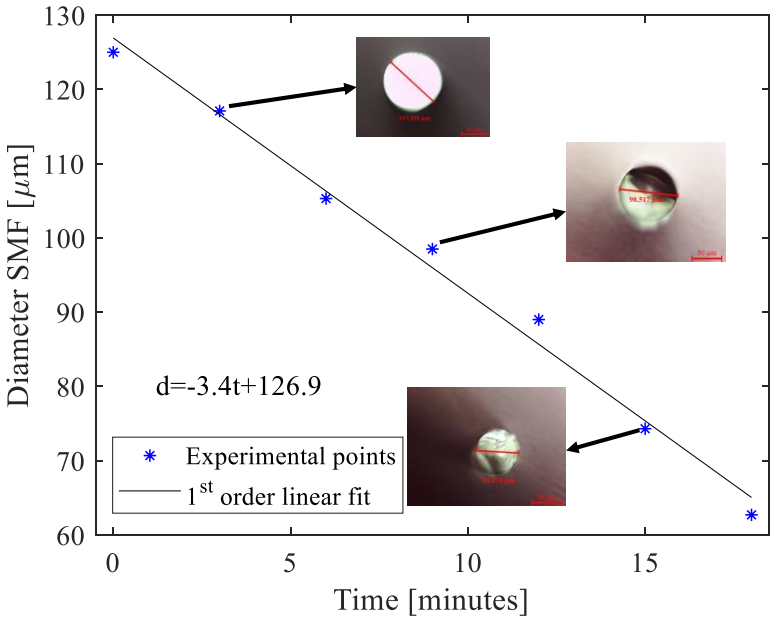

Figure 23. Variation of the diameter of the SMF during the etching process in HF (48 %).

After applying a 1st order linear fit to the data points presented in Figure 23, it was obtained an etching rate of 3.4 μm/min. With this information it was decided to submerge the SMF for a period of 19 minutes. This was the time chosen to etch the unprotected areas to a diameter of about 60 μm.

4.1.3. Strain induced long period grating characterization

In order to induce a periodic refractive index modulation along the length of the fiber, the structure was subjected to strain. This was done through a linear positioner from Thorlabs, Inc., with 15 mm range and 10 μm resolution. The fiber structure was secured between two fiber clamps, one sitting on top of the linear positioner and another fixed onto a pedestal pillar post. The strain characterization was made using the setup shown on Figure 24.

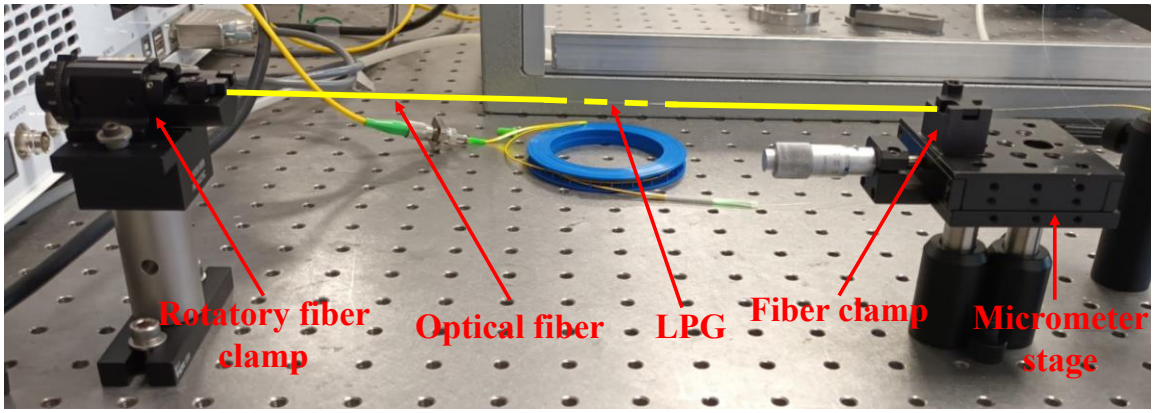

Figure 24. Experimental setup used to do the strain characterization.

The distance between the fiber clamps shown on the setup of Figure 24 was L = 24.2 cm. Considering the elastic limit of the SMF as ε = 7000 με, it could be determined the maximum

length variation supported by the fiber, which was $dl_{max} = \varepsilon * L \approx 1.7$ cm. To avoid breaking the fiber, the strain was applied in steps of 207 με up to a maximum of 6612 με. The spectral characterization was made by launching light from a supercontinuum laser source (Fianium WhiteLase™ SC480-20), into the fiber and measuring the transmission spectrum through an optical spectral analyser (OSA), reference AQ6375E, from Yokogawa. The spectra were acquired at each strain step.

4.1.4. Curvature induced long period grating / displacement characterization

When the fiber is bent, a periodic strain distribution will alter the refractive index of the fiber structure as reported in section 2.2.2. The strength of the periodic strain distribution depends on the curvature imposed on the fiber structure and this can be adjusted by placing the corrugated structure in a loop, where one of the terminals is fixed while the other is allowed to move. The loop was easily created by passing the two fiber terminals through a plastic pipe with 1 mm inner diameter. The periodic etched fiber structure was kept in the middle region of the loop. Since the optical fiber was only etched at the region given by the length of the periodic structure, the shape acquired by the whole fiber structure was similar to that of a balloon. To perform the displacement characterization, one terminal of the fiber structure was fixed with glue to a stationary platform and the other terminal was moved in steps of 5 mm up to 135 mm. The transmission spectra were acquired for each displacement step. The representative scheme of this characterization process can be seen in Figure 25(a), while a picture of the implemented setup on Figure 25(b).

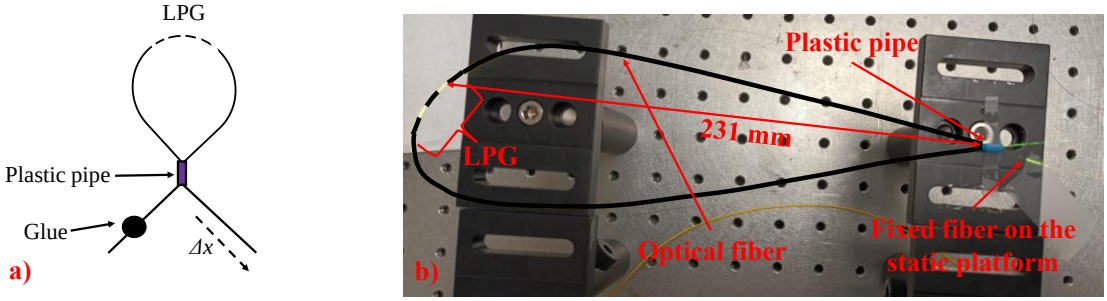

Figure 25. a) Representative scheme of the experimental setup used to characterize the corrugated structure to displacement. b) Experimental setup used to characterize the corrugated structure. The black dashed trace was drawn for clarity, namely, to indicate the shape defined by the optical fiber.

4.1.5. Temperature characterization of the corrugated long period grating

The fiber configuration used on the temperature characterization considered the balloon like shape structure used in the previous section for the displacement characterization. However, in this characterization, the two fiber terminals were glued in a position such that the shape of the balloon allow the appearance of a spectral resonance in the transmission spectrum. After this process, the fiber was placed inside a recipient filled with water and inserted in a thermal bath chamber (LAUDA Eco Silver RE 415) also filled with water. This was done in order to avoid the turbulences of the water flow inside the chamber, which create noise in the transmission spectra. The temperature test was made for temperatures starting at 21 ºC and finishing at 35 ºC, in steps of 2 ºC. For each step of temperature, it was necessary to wait approximately 3 minutes to let the temperature at the thermal chamber to stabilise. After this period, the transmission spectra were acquired.

4.2. Long period gratings results

4.2.1. Analysis of the comb-like structure

After the 3D printing of the comb-like structure, it was decided to analyse the structure under an optical microscope. In this analysis, it was evaluated the periodicity of the comb and diameter of the teeth of the comb-like structure. The images regarding this this evaluation can be seen on Figure 26.

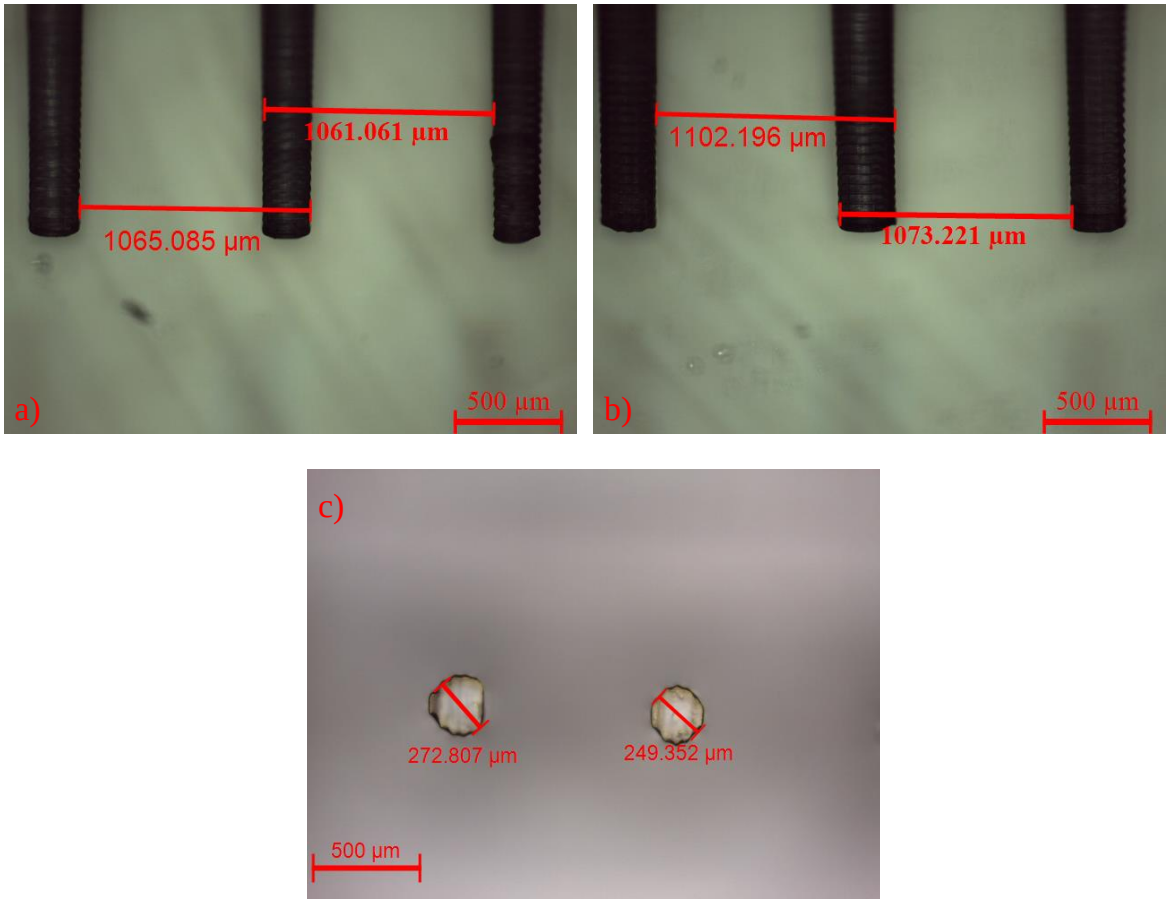

Figure 26. a), b) Transversal and c) top view microscope images of the protruded cylinders of the comb-like structure. In a) and b) it is shown the period of the teeth and in c), their diameter.

As observed from the figure above, the period of the comb-like structure reached values ranging from ~1061 up to ~1102 µm, which is not equal to the one projected on the drawing software, i.e. 1060 µm. An explanation for such discrepancy may result from the soft nature of the polymer resin that allow the protruded structures to tilt. A problem that is magnified for longer and thinner protruded cylinder structures. Also, the top view microscope images shown in Figure 26 c), demonstrate some inconsistencies regarding the projected and the measured values, i.e. 200 µm vs. ~240 to 273 µm, respectively. Furthermore, the shape is not completely round as was projected. The dimensions and shape deviations between the projected and the ones observed on Figure 26, are mainly associated to the resolution of 3D printer, i.e 47 µm in the xy dimensions, yelding a pixelated structure as observed in Figure 26c) and periods higher than the ones predicted. The observed deviations can cause errors in

the production process of the corrugated LPGs, and consequently, to the exact wavelength location of resonances.

The results regarding the microscope images of the resin periodically transferred to the optical fiber for designed grating periods of 700 μm, 750 μm, 800 μm and 850 μm are shown in Figure 27.

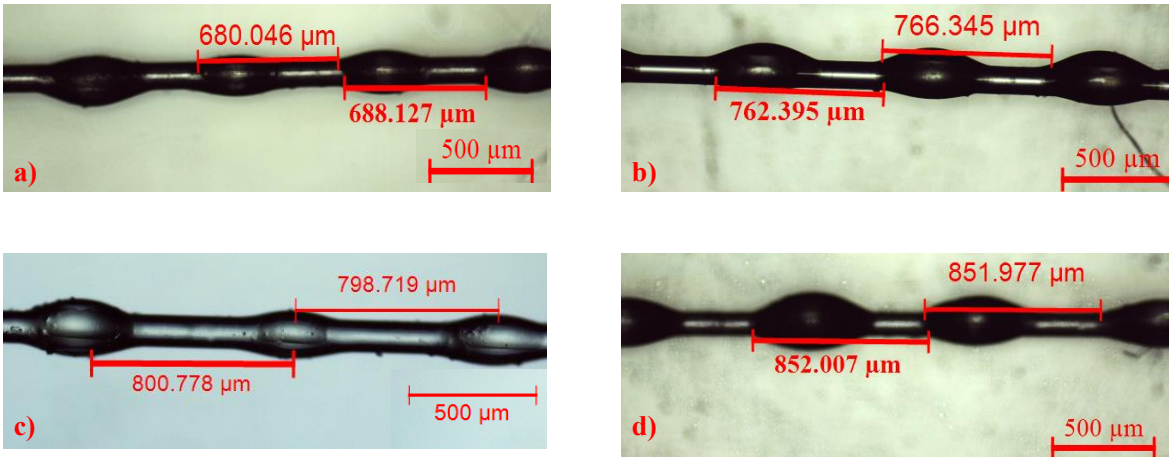

Figure 27. Periodic distribution of the liquid resin along the length of the fiber for the gratings with periods of a) 700 μm, b) 750 μm, c) 800 μm and d) 850 μm.

As is seen from Figure 27, the resin was periodically distributed along the length of the SMF for the four samples. The regions covered with the liquid resin appear with an ellipsoidal shape due to the surface tension between the liquid resin and the SMF surface. The measurements taken for the period of the resin structure, show some degree of error between the predicted and the measured values. Again, the reason was related to the printer resolution and the thickness and length of the protruded cylindrical structures. However, during the resin deposition it is possible the existence of another source of error, namely the one associated to the movement of the resin drops on the surface of the optical fiber. This source of error can be minimized with high viscosity resins; avoid possible sources of air flows; and keeping the fiber straight to keep the gravity forces acting perpendicular to the length of the fiber. These were all parameters that have been taken into account in this work, either through the use of different liquid resins, use of non-ventilated areas and the use of a multiaxis positioner to maintain the fiber levelled.

Having verified that the resin is periodically distributed on the optical fibers, it is then possible to carry out the etching process on the optical fibers.

4.2.2. Analysis of the corrugated LPG structure

After the UV hardening of the periodic liquid resin structures, the etching of the fiber was followed. The results can be seen in Figure 28.

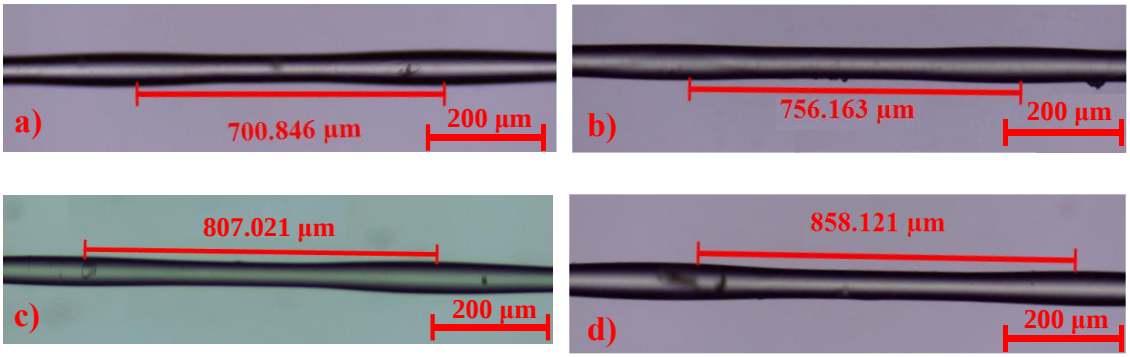

Figure 28. Microscope images (observed under a 10 X objective) of the periodic fiber resin structure after HF etching (48%) after 19minutes exposure. The results were obtained for structures with periods of, a) 700 µm, b) 750 µm, c) 800 µm and d) 850 µm.

As it can be seen from Figure 28, the SMFs present a slightly undulated shape along its length. These slightly differences were associated to the gradient etching that took place between the unprotected and protected regions of the fiber. This allowed to have a higher corrosion depth for the unprotected regions compared to the ones protected by the photopolymerizable resin. To quantify the diameter difference between these regions, microscope images of a higher magnification were also taken. The results are shown in Figure 29 for the etched fiber structure with period of 700 µm.

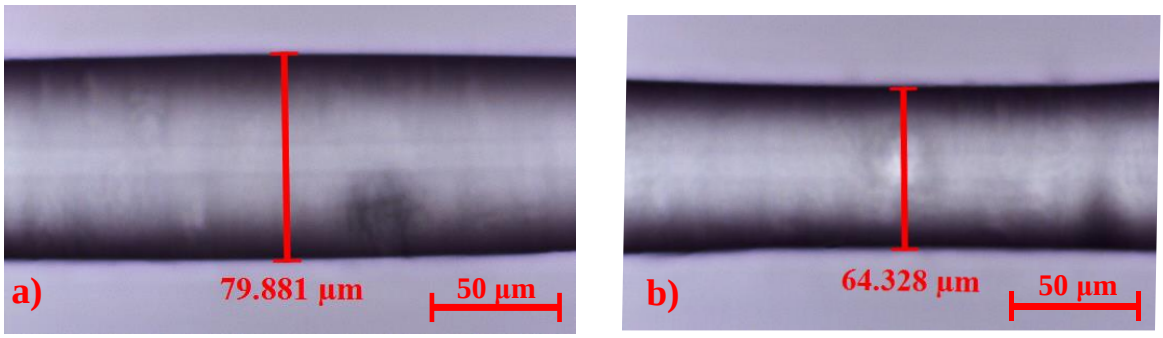

Figure 29. Microscope images (observed under 50 X objective) of the protect and unprotected fiber regions of the 700 µm period structure presented in Figure 27a) and Figure 28a). The etching was done in HF (48%) for an exposure time of 19 minutes.

As it can be seen from Figure 29, the etching process resulted in fiber diameters of ~80 µm for the region "protected" by the resin, and ~64 µm (predicted diameter of ~62 µm from Figure 23) for the regions exposed to the acid. This gives a diameter difference of approximately 16 µm. According to the theoretical curve fitting found in Figure 23, this 15 µm difference corresponds to about 4.7 minutes of protection. The reason for such small value is associated to the adhesion of the resin to the silica material that composes the GOF, judging the results, it can be said that the adhesion is not strong enough to survive the HF chemical attack. It must be stressed that other commonly used photopolymerizable resins

from other manufactures and with different formulations have also been tested and similar results have been reached.

4.2.3. Strain induced long period grating – characterization results

Following the experimental procedure described in section 4.1.3, the corrugated structure was subjected to a longitudinal strain test. The periodic structure chosen for this first test was the one with a period of 750 µm. The results of this characterization can be seen on Figure 30.

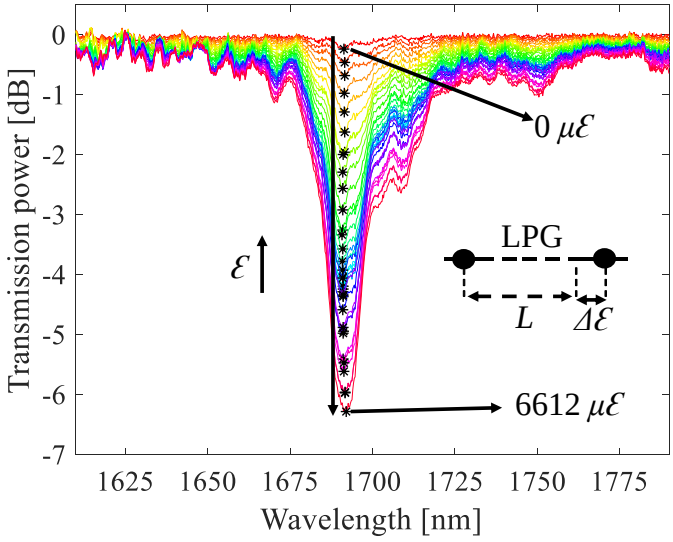

Figure 30. Transmission spectra obtained for the strain characterization regarding the 750 µm period grating.

When the corrugated structure is not under any external load, the spectrum presents a flat spectral response with 0 dB losses. Under such conditions, the periodic diameter changes on the fiber are not able to affect the refractive index of the fiber's core and thus, the spectrum is not affected. However, when the corrugated structure is subjected to an external load, such as longitudinal strain as explored in Figure 24, an attenuation band appears at the wavelength of ~1695 nm. This band corresponds to the coupling of the fundamental core mode to the higher order cladding mode. The coupling strength of this attenuation band increases as the strain increases, as a consequence of the increase of the refractive index change between the regions with higher and lower fiber diameters. This effect happens due to the strain-optic effect previously described in equation (10). Important characteristics of this spectral filter is the low out-of-band loss (< 0.3 dB), and an apparent stabilization of the resonance wavelength during the strain characterization. When the corrugated structure is subjected to a strain amount of 6612 µε, the structure presents a core to cladding coupling strength of ~6.2 dB (76 %), and 3 dB bandwidth of 11 nm. In order to fully understand the power and wavelength dependence of the structure with the strain applied, the dip power wavelength was measured as is shown by the star markers in Figure 30. The compilation of the results can be seen in Figure 31.

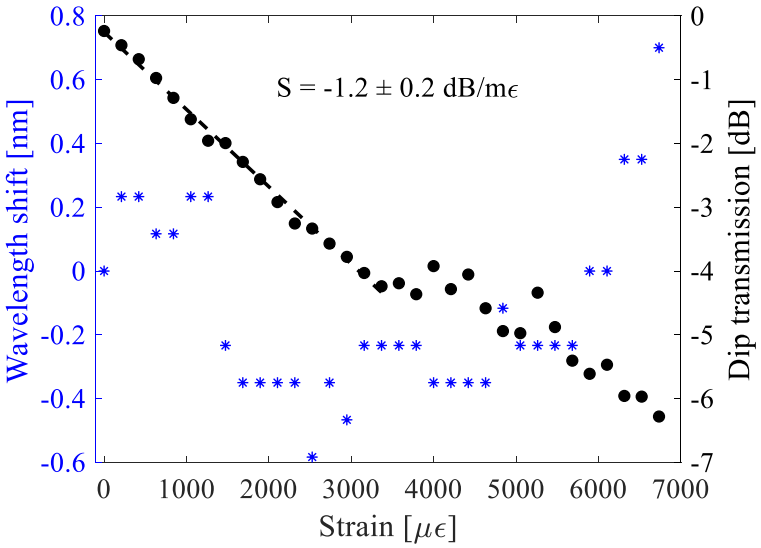

Figure 31. Dip power and dip wavelength shift as function of strain for the 750 µm grating.

From the figure above, it is possible to verify that when the strain increases, the dip power also increases. It can be also verified that there is a linear correlation between the strain and the dip power for strain values between 0 µε and 3370 µε. The sensitivity obtained from a first order linear fit applied to the data points revealed a sensitivity of -1.2 ± 0.2 dB/mε. This shows that additionally to the filtering characteristics of the corrugated structure, it is also possible to use this structure to measure strain through optical power detection schemes.

The sensitivity obtained for this sensor (-1.2 dB/mε), is slightly higher than the ones reported in literature for similar corrugated structures -1.1 dB/mε [73]. So, despite the sensitivity to strain was not the main advantage of the corrugated structure reported in this work, this dispositive also has that advantage over the other sensors reported in the literature. To achieve even higher sensitivities to the strain tests, it would be necessary to improve the adhesion process between the fiber and the resin, which will allow to reach higher modulation depths, which will generate higher refractive index modulations at lower strains. To reach that, the fiber could need to be treated in a piranha solution, allowing an enhancement of the resin adhesion.

In addition to the dip power, Figure 31 also presents the dip wavelength shift as function of strain. However, in this case, there is no correlation between the dip wavelength shift and the applied strain, being the maximum deviation observed of ~1.05 nm. For the range of interest, namely for the linear region presented for the dip power characterization (between 0 µε and 3370 µε), it can be seen that the maximum wavelength deviation is ~0.7 nm. Considering that the bandwidth of the resonance band is ~4.2 dB, it can be concluded that the corrugated structure is a promising device to be used in cost effective and real-time sensor applications, namely through the use of a laser centered at the resonance wavelength as the input source and a photodetector at the output.

In order to check the tunability of the resonance wavelength, as function of the grating period, the corrugated fiber structures presented in Figure 28, namely with periods of 700,

750, 800 and 850 µm, were subjected to a longitudinal strain of ~6500 µε. The transmission spectra of the gratings can be seen on Figure 32.

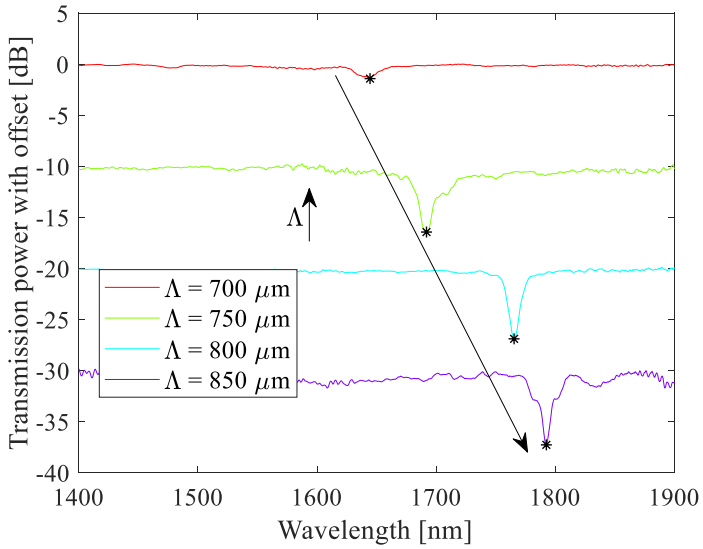

Figure 32. Transmission spectra of different gratings (700 : 50 : 850) obtained when the corrugated structure was under a longitudinal strain of 6500 µε. The spectra are separated with an offset of 10 dB.

As it can be seen from the figure above, all the gratings present only one attenuation band for the wavelength region between 1400 and 1900 nm. Their coupling strength is similar to all of them, reaching values of ~6 to 7 dB, except for the grating of 700 µm, which shows a coupling strength of ~1.5 dB. The weaker coupling strength observed for the 700 µm period corrugated LPG, prove that for gratings smaller or equal to this period, the periodic liquid resin cannot be periodically distributed along the fiber.4.1.2

One important thing to notice in Figure 32 is related to the different resonance wavelengths reached for each of the periodic structures. The relation seems to be linear, showing a higher wavelength resonance for higher grating periods. This is important, since the structure fabricated in this work shows the capability to be tuned in both power and wavelength, showing promising opportunities as a spectral filter. In order to understand the dependence between the grating period and the attenuation band, the dip power wavelength of each attenuation band was measured and the graph of the period as function of the resonance wavelength was plotted as is shown in Figure 33.

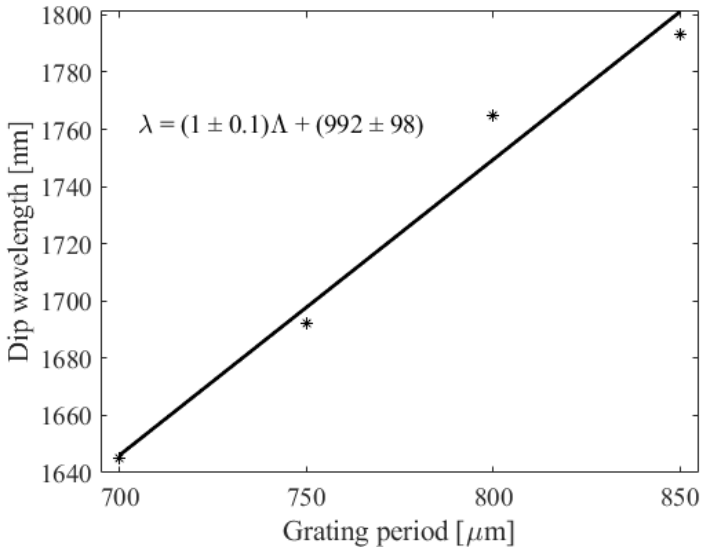

Figure 33. Resonance wavelength as a function of the grating period.

The results shown in Figure 33, reveal that there is a linear correlation of the resonance wavelength with the period of the grating for the wavelengths under analysis. Yet, for other wavelength spans, the phase matching curve needs to be analysed. By adjusting a first order linear fit to the experimental data points, it was possible to reach the following equation $\lambda = (1 \pm 0.1) * \Lambda + (922 \pm 98)$, showing an easy way to tune the wavelength of the filter.

4.2.4. Displacement induced long period grating – characterization results

The displacement characterization was made for the corrugated structure with the period of 750 µm. The graph of the optical power as a function of wavelength can be seen on Figure 34:

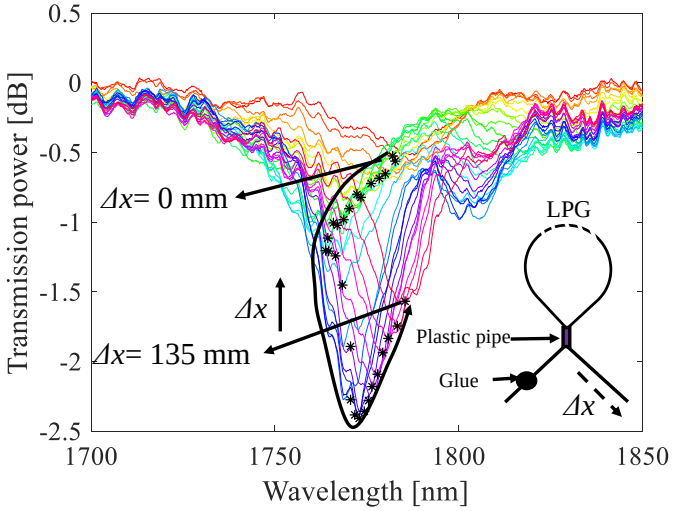

Figure 34. Transmission spectra of a 750 µm period corrugated structure, when different steps of displacements are applied. The scheme of the displacement setup is shown in the right side of the image.

As shown in Figure 34, the spectral dip loss changed both in power and wavelength with increasing displacement. One interesting thing to notice is the wavelength location of the resonance, which now appeared at ~1770 - 1790 nm, which is a shift of ~80 to 100 nm

to the right compared to the one reached for the strain characterization (i.e. 1695 nm), observed for the same corrugated structure, Figure 30. It was observed that depending on the region where the grating was on the balloon-like structure, the resonance wavelength could be located in different regions of the spectra in a range of ~150 nm. So, it can be suspected that the reason for such behaviour is related to the different mechanical stresses involved, allowing to satisfy the phase-matching condition for other wavelengths. Also, the grating growth strength observed in Figure 34 is non-linear contrary to what was observed for the strain test. In the displacement characterization, the spectra were blue-shifted for small displacements and red-shifted for large displacements. By tracking the dip power resonance, as shown in Figure 34 by the star marker points, it was possible to get the dip power and dip wavelength shift as function of displacement as is seen in Figure 35.

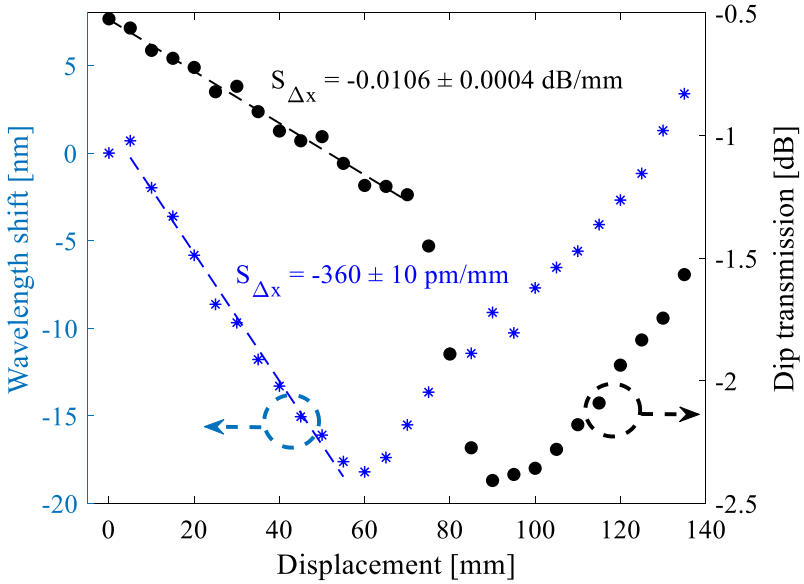

Figure 35. Dip wavelength shift and dip power as function of displacement.

From Figure 35, it can be seen a linear response of the dip power and dip wavelength shift for displacement values up to ~60 to 70 mm. The slopes reached for those were ~0.011 dB/mm and 360 pm/mm, respectively. After this linear region, the coupling strength increases at a fast rate up to ~90 mm, followed by a slightly linear response up to the end of the characterization (i.e. 140 mm). Regarding the dip wavelength shift, the negative slope observed up to ~60 mm changed to a positive wavelength shift slope after this region. One possible reason for this change of behaviour could be associated with the satisfaction of the phase-match condition for other wavelengths. Yet, further studies are required to investigate the cause. However, it is important to emphasize the capability to measure displacement either in power or wavelength over a dynamic range wider than that found in the literature (i.e. 2.125 mm [74]), which to the best of my knowledge is the first of this type using grating structures.

4.2.5. Results of the temperature characterization

The results concerning the temperature characterization of the corrugated LPG with period of 750 µm and bent in a balloon-like shape as indicated on the previous section, can be seen in Figure 36.

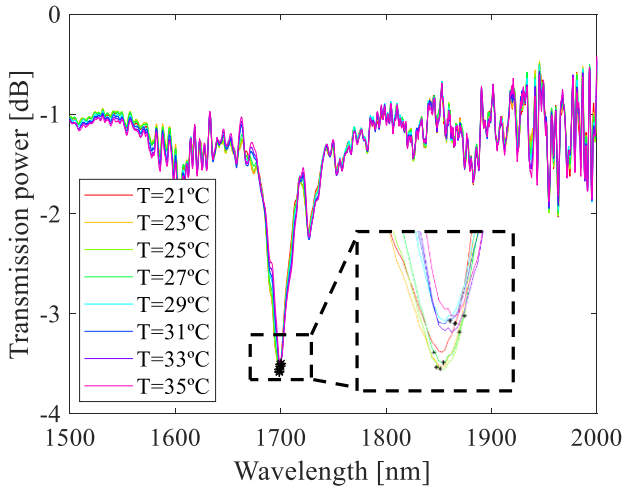

Figure 36. Transmission spectra obtained at different temperature steps.

Figure 36 shows that the spectra suffered a red-wavelength shift with increasing temperature. It also shows that the resonance band appears at the wavelength of ~1700 nm, which was different from the one found in Figure 34 for the displacement characterization (i.e. 1770 - 1790 nm), but closer to the one reached for the strain characterization (i.e. 1690 nm) shown in Figure 30. Again, the reason was associated to the location of the corrugated LPG on the balloon-like structure. The out-of-band losses (~1 dB) presented in these spectra were associated to the losses of the connectors and cables added to the measurement setup after the signal normalization process. However, for the purpose of the characterization this is irrelevant.

By taking the dip power at the wavelength of 1700 nm, it was possible to see the relation between wavelength shift as well as the dip power with the change of temperature. These results can be seen in Figure 37.

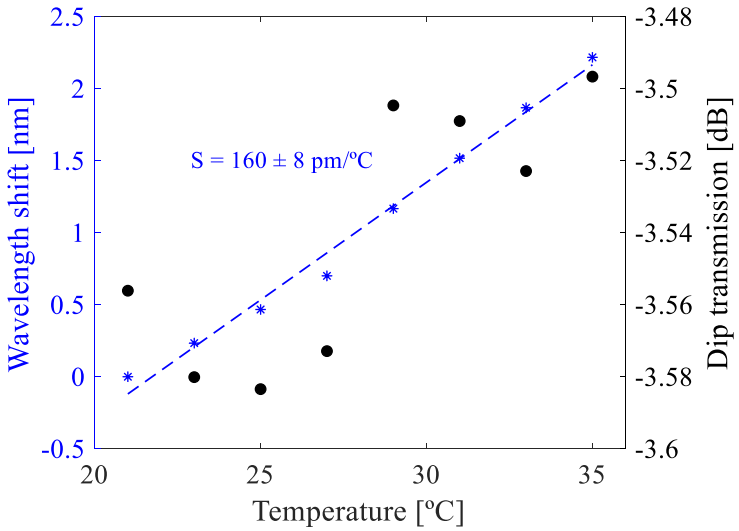

Figure 37. Dip wavelength shift and dip power as function of temperature.

As shown in Figure 37, the corrugated LPG presents a linear wavelength shift response with increasing temperature. Thus, a first order linear fit was applied to the experimental data points. The results showed a sensitivity of 160 ± 8 pm/°C, proving that it is possible to monitor temperature with this structure through wavelength detection approaches. Considering the use of the corrugated structure for displacement sensor applications, the temperature cross sensitivity would be ~160/360 = 0.44 mm/ºC, which demonstrates the necessity to implement compensation schemes to operate this sensor in an environment with temperature fluctuations. An approach could be done through the simultaneous usage of both wavelength and dip power detection approaches.

Regarding the value obtained for the temperature sensitivity, it was found that it was higher than the one reported in the literature for similar corrugated structures, which present a sensitivity of 58.4 pm/ºC [53]. This is approximately three times lower than the one reached in this work. The explanation for such difference is associated to the change of the effective refractive index of the cladding mode with the temperature. The cladding mode resonance reported in [53] and the one found in this work are probably different, and thus, their sensitivities are expected to be also different.Concerning the results obtained for the dip power as function of temperature, it can be seen from Figure 37, that there is no correlation between the data, showing a negligible power change with temperature (i.e. maximum deviation of 0.09 dB). This becomes relevant for the strain sensor as it operates through optical power detection schemes. Thus, a maximum error of ~0.09/0.0012=75 με is expected to be obtained for the strain sensor operation range between 0 με and 3370 με.

5. Conclusion

This thesis dedicated to the fabrication and applications of two different fiber optic sensors, namely multimodal interferometers and long period gratings, using fiber post-processing techniques.

In the first part of this work, glass optical fiber multimodal interferometers and polymer optical fiber multimodal interferometers were fabricated and tested for hydrostatic pressure measurements. The results obtained for both sensors were satisfactory, since it was verified that both sensors were able to monitor the hydrostatic pressure through the analysis of the spectral wavelength shift. The results revealed a sensitivity of -4.6 pm/bar for the glass optical fiber multimodal interferometers, which is identical to the one reported in literature for few-mode fiber, (i.e. 2.4 pm/bar). Regarding the polymer optical fiber multimodal interferometers response, it was obtained a sensitivity of 58 pm/bar. This sensitivity revealed a twelve-fold sensitivity increase when compared to the glass optical fiber multimodal interferometers results. These results were associated to polymer optical fiber higher Poisson's ratio (~0.35 vs. ~0.17), and the much lower Young's modulus (23 times), allowing it to reach higher deformations and higher refractive index changes for the same amount of pressure. As a consequence of the etching process done in the polymer optical fiber, necessary to easily fuse the glass optical fiber and polymer optical fiber terminals during the assembly of the polymer optical fiber multimodal interferometer, the core of the polymer optical fiber become exposed to the external environment. Simulation results revealed that the oil-pump refractive index induces changes of 0.34 pm/bar, which corresponds to a deviation of ~0.6 %/bar which can be considered acceptable for pressure changes.

With these results it was concluded that the polymer optical fiber multimodal interferometer is a good option to measure hydrostatic pressure, since it presents better sensitivity results than the glass optical fiber multimodal interferometer and also better than the ones reported in literature for polymer optical fiber Bragg gratings. Another factor that is favorable to this sensor is related to its simplicity of production and the low-cost associated to its production. Regarding the applicability of this sensor, it is important to mention that demodulation techniques based on power would be more interesting than the wavelength detection schemes used in this work. However, these can be easily explored through the use of the edge filtering technique, namely by tuning a laser at the edges of the filter and monitoring the output power. Changes in the spectra wavelength could then be converted into optical power changes, which offer not only reduced costs but also real time detection.

The second part of this work was devoted to the post-processing of a single-mode glass optical fiber to a corrugated structure, namely to the development of an induced long period grating. To obtain the corrugated structure a comb-like structure was 3D printed. This was used to periodically distribute a photopolymerizable resin on the surface of an optical fiber. Depending on the angle in which the comb-like structure passes through the fiber, this will influence the final period of the grating structure. After this, the structure was subjected to HF chemical attack, allowing to create a structure with a periodic etch depth. Next, the response of the structure was observed for different parameters, namely strain, displacement, and temperature.

Before the characterizations, the spectra appear with a 0 dB flat response because of the absence of external stresses acting on the fiber. However, when subjected to external loads the appearance of an attenuation band was observed. This corresponded to the core to cladding mode coupling and it was associated to the refractive index modifications imposed on the fiber as consequence of the strain-optic effect associated to the different stresses observed along the corrugated structure. Specifically talking on the strain test, it was verified a linear correlation between the dip power of the resonance band and the longitudinal strain applied to structure. Concerning the dip wavelength shift, there was no evident correlation, presenting a maximum wavelength change of ~1.1 nm for the linear span range of the dip power characterization. Considering the large bandwidth of the resonance band (11 nm), this brings an interesting opportunity regarding the use of the sensor in real-time and low-cost detection schemes through intensity detection schemes. This could be easily complemented through the use of a laser centered at the attenuation band wavelength and a photodetector at the output. Still on the strain characterization tests, it was also verified that there is a correlation between the period of the grating and the wavelength where the attenuation band appears, following a linear relationship, i.e. $\lambda = (1 \pm 0.1) * \Lambda + (922 \pm 98)$. This proves that the corrugated long period grating produced in this thesis can be tuned to a specific wavelength through the manipulation of the period during the production process. The phase match curve was extrapolated for the periods ranging between 700 and 850 nm, however, for other wavelength ranges it would be necessary the study of the response of the phase matching curve.

The second characterization was related to the displacement. In this test the fiber structure was mounted in a balloon-like shape, allowing to bend the fiber structure and thus modulate its refractive index. In this characterization, one fiber terminal as fixed and the other was linearly displaced, allowing to subject the structure to different curvatures. It was verified that the attenuation band increases with the increasing of the displacement until a displacement of 60 mm, after this, the coupling strength starts to decrease, and the attenuation band becomes weaker. However, a new attenuation band starts to appear near to the first one. This could be happening due to the fact that the phase-match condition is being satisfied for other wavelengths. The calibration of the results revealed a sensitivity of 360 pm/mm and 0.011 dB/mm for the dip wavelength and dip power in a wide displacement range when compared to the literature, i.e. 2 mm [74]. This makes the sensor very promissory to be used in large range displacement sensor applications.

For the last characterization, the balloon-like structure was used and fixed at a position that allowed to observe the attenuation band. The temperature characterizations revealed a negligible optical power variation of the attenuation bandwidth with the change of temperature (i.e. ~0.09 dB in a 14ºC temperature span), proving that the temperature has little influence in the optical power of the attenuation band. For the wavelength shift, it was proved that there was a linear correlation between the temperature and the dip wavelength shift, showing sensitivities of 160 pm/ºC. This linear relationship shows that it is possible to use the corrugated structure in temperature related applications. Despite the possibility in using the corrugated structure as temperature sensor based on wavelength changes, the most

important conclusion about this characterization is the cross-sensitivity issues that temperature can have in the strain and temperature characterization. It can induce errors of ~75 με in the strain characterization. Considering that, it should be used some compensation schemes need to be implemented. However, considering that the sensor can in some cases operate in dip power and dip wavelength a sensitivity matrix could be used to solve the problem.

References

[1] M. Arumugam, “Optical fiber communication - An overview,” *Pramana - J. Phys.*, vol. 57, no. 5–6, pp. 849–869, 2001, doi: 10.1007/s12043-001-0003-2.

[2] J. Li, E. Lindholm, J. Horska, and J. Abramczyk, “Advances in design and development of optical fibers for harsh environments,” *Int. Wire \& Cable Symp.*, no. 860, pp. 1–12, 1999.

[3] I. García, J. Zubia, G. Durana, G. Aldabaldetreku, M. A. Illarramendi, and J. Villatoro, “Optical fiber sensors for aircraft structural health monitoring,” *Sensors*, vol. 15, no. 7, 2015, doi: 10.3390/s150715494.

[4] A. F. Da Silva, A. F. Gonçalves, P. M. Mendes, and J. H. Correia, “FBG sensing glove for monitoring hand posture,” *IEEE Sens. J.*, vol. 11, no. 10, pp. 2442–2448, 2011, doi: 10.1109/JSEN.2011.2138132.

[5] E. Vorathin, Z. M. Hafizi, N. Ismail, and M. Loman, “Review of high sensitivity fibre-optic pressure sensors for low pressure sensing,” *Opt. Laser Technol.*, vol. 121, 2020, doi: 10.1016/j.optlastec.2019.105841.

[6] X. Zhou, Q. Yu, and W. Peng, “Fiber-optic Fabry–Perot pressure sensor for down-hole application,” *Opt. Lasers Eng.*, vol. 121, pp. 289–299, 2019, doi: 10.1016/j.optlaseng.2019.04.028.

[7] L. Wang, Y. Wang, J. Wang, and F. Li, “A High Spatial Resolution FBG Sensor Array for Measuring Ocean Temperature and Depth,” *Photonic Sensors*, vol. 10, no. 1, pp. 57–66, 2020, doi: 10.1007/s13320-019-0550-0.

[8] S. Zhang *et al.*, “An optical fiber pressure sensor with ultra-thin epoxy film and high sensitivity characteristics based on blowing bubble method,” *IEEE Photonics J.*, vol. 13, no. 1, 2021, doi: 10.1109/JPHOT.2021.3055872.

[9] Y. Haseda, J. Bonefacino, H. Y. Tam, S. Chino, S. Koyama, and H. Ishizawa, “Measurement of pulse wave signals and blood pressure by a plastic optical fiber FBG sensor,” *Sensors*, vol. 19, no. 23, 2019, doi: 10.3390/s19235088.

[10] F. Li, Y. Du, W. Zhang, and F. Li, “Fiber Bragg grating soil-pressure sensor based on dual L-shaped levers,” *Opt. Eng.*, vol. 52, no. 1, p. 014403, 2013, doi: 10.1117/1.oe.52.1.014403.

[11] R. Oliveira, L. Bilro, and R. Nogueira, “Fabry-Pérot cavities based on photopolymerizable resins for sensing applications,” *Opt. Mater. Express*, vol. 8, no. 8, pp. 2208–2221, 2018, doi: 10.1364/ome.8.002208.

[12] Y. Zhang, L. Yuan, X. Lan, A. Kaur, J. Huang, and H. Xiao, “High-temperature fiber-optic Fabry–Perot interferometric pressure sensor fabricated by femtosecond laser,” *Opt. Lett.*, vol. 38, no. 22, pp. 4609–4612, 2013, doi: 10.1364/ol.38.004609.

[13] R. Oliveira, L. Bilro, T. H. R. Marques, C. M. B. Cordeiro, and R. Nogueira, “Strain sensitivity enhancement of a sensing head based on ZEONEX polymer FBG in series with silica fiber,” *J. Light. Technol.*, vol. 36, no. 22, pp. 5106–5112, 2018, doi: 10.1109/JLT.2018.2870054.

[14] R. Oliveira, T. H. R. Marques, L. Bilro, R. Nogueira, and C. M. B. Cordeiro, “Multiparameter POF Sensing Based on Multimode Interference and Fiber Bragg Grating,” *J. Light. Technol.*, vol. 35, no. 1, pp. 3–9, 2017, doi: 10.1109/JLT.2016.2626793.

[15] X. Fan, J. Jiang, X. Zhang, K. Liu, S. Wang, and T. Liu, “Multimode interferometer-based torsion sensor employing perfluorinated polymer optical fiber,” *Opt. Express*, vol. 27, no. 20, pp. 28123–28132, 2019, doi: 10.1364/OE.27.028123.

[16] Y. Gong, T. Zhao, Y. J. Rao, and Y. Wu, “All-fiber curvature sensor based on

multimode interference," *IEEE Photonics Technol. Lett.*, vol. 23, no. 11, pp. 679–681, 2011, doi: 10.1109/LPT.2011.2123086.
[17] J. Rafael Guzman-Sepúlveda, R. Guzman-Cabrera, and A. Alberto Castillo-Guzmán, "Optical Sensing Using Fiber-Optic Multimode Interference Devices : A Review of Nonconventional Sensing Schemes," *Sensors*, vol. 21, 2021, doi: https://doi.org/10.3390/s21051862.
[18] D. Chen, C. Wu, M.-L. V. Tse, and H. Y. Tam, "Hydrostatic pressure sensor based on mode interference of a few mode fiber," *Prog. Electromagn. Res.*, vol. 119, pp. 335–343, 2011, doi: 10.2528/PIER11071001.
[19] K. Peters, "Polymer optical fiber sensors - A review," *Smart Mater. Struct.*, vol. 20, p. 013002, 2011, doi: 10.1088/0964-1726/20/1/013002.
[20] R. Oliveira, L. Bilro, and R. Nogueira, "Polymer Optical Fiber Sensors and Devices," in *Handbook of Optical Fibers*, 1st ed., G. Peng, Ed. Springer, 2019, pp. 1–41.
[21] R. Min *et al.*, "Chirped POF Bragg grating production utilizing UV cure adhesive coating for multiparameter sensing," *Opt. Fiber Technol.*, vol. 65, p. 102593, 2021, doi: 10.1016/j.yofte.2021.102593.
[22] I. P. Johnson, D. J. Webb, and K. Kalli, "Hydrostatic pressure sensing using a polymer optical fibre Bragg gratings," *Third Asia Pacific Opt. Sensors Conf.*, vol. 8351, p. 835106, 2012, doi: 10.1117/12.914391.
[23] K. Bhowmik *et al.*, "Experimental study and analysis of hydrostatic pressure sensitivity of polymer fibre Bragg gratings," *J. Light. Technol.*, vol. 33, no. 12, pp. 2456–2462, 2015, doi: 10.1109/JLT.2014.2386346.
[24] J. Witt, M. Breithaupt, J. Erdmann, and K. Krebber, "Humidity sensing based on microstructured pof long period gratings," *POF 2011 20th Int. Conf. Plast. Opt. Fibers - Conf. Proceeding*, pp. 409–414, 2011.
[25] I. Chapalo, A. Theodosiou, K. Kalli, and O. Kotov, "Multimode Fiber Interferometer Based on Graded-Index Polymer CYTOP Fiber," *J. Light. Technol.*, vol. 38, no. 6, pp. 1439–1445, 2020, doi: 10.1109/JLT.2019.2954286.
[26] X. Fan, J. Jiang, X. Zhang, K. Liu, S. Wang, and T. Liu, "Multimode interferometer-based torsion sensor employing perfluorinated polymer optical fiber," *Opt. Express*, vol. 27, no. 20, pp. 28123–28132, 2019, doi: 10.1364/oe.27.028123.
[27] G. Statkiewicz-Barabach, D. Kowal, M. K. Szczurowski, P. Mergo, and W. Urbanczyk, "Hydrostatic pressure and strain sensitivity of long period grating fabricated in polymer microstructured fiber," *IEEE Photonics Technol. Lett.*, vol. 25, no. 5, pp. 496–499, 2013, doi: 10.1109/LPT.2013.2244590.
[28] A. M. Vengsarkar, N. S. Bergano, C. R. Davidson, J. R. Pedrazzani, J. B. Judkins, and P. J. Lemaire, "Long-period fiber-grating-based gain equalizers," *Opt. Lett.*, vol. 21, no. 5, pp. 336–338, 1996, doi: 10.1364/ol.21.000336.
[29] X. J. Gu, "Wavelength-division multiplexing isolation fiber filter and light source using cascaded long-period fiber gratings," *Opt. Lett.*, vol. 23, no. 7, pp. 509–510, 1998, doi: 10.1364/ol.23.000509.
[30] S. Ramachandran, Z. Wang, and M. Yan, "Bandwidth control of long-period grating-based mode converters in few-mode fibers," *Opt. Lett.*, vol. 27, no. 9, pp. 698–700, 2002, doi: 10.1364/ol.27.000698.
[31] V. Bhafia and A. M. Vengsarkar, "Optical Fiber Long-Period Grating Sensors," *Opt. Lett.*, vol. 21, no. 9, pp. 692–694, 1996, doi: 10.1364/OL.21.000692.
[32] J. K. Bae, S. H. Kim, J. H. Kim, S. B. Lee, J. M. Jeong, and J. H. Bae, "Spectral

Shape Tunable Band-Rejection Filter Using Long Period Fiber Gratings with Divided Coil Heater," *IEEE Photonics Technol. Lett.*, vol. 15, no. 3, pp. 407–409, 2003, doi: 10.1109/LPT.2002.807955.

[33] M. Deng *et al.*, "Long period fiber grating based on periodically screw-type distortions for torsion sensing," *Opt. Express*, vol. 25, no. 13, pp. 14308–14316, 2017, doi: 10.1364/oe.25.014308.

[34] N. F. Valente, L. Bilro, and R. Oliveira, "3D printing of long period gratings for curvature applications," vol. 255, p. 12001, 2021, doi: https://doi.org/10.1051/epjconf/202125512001.

[35] Y.-P. Wang, L. Xiao, D. N. Wang, and W. Jin, "Highly sensitive long-period fiber-grating strain sensor with low temperature sensitivity," *Opt. Lett.*, vol. 31, no. 23, pp. 3414–3416, 2006, doi: 10.1364/OL.31.003414.

[36] S. Khaliq, S. W. James, and R. P. Tatam, "Enhanced sensitivity fibre optic long period grating temperature sensor," *Meas. Sci. Technol.*, vol. 13, pp. 792–795, 2002, doi: 10.1109/OFS.2002.1000521.

[37] T. Venugopalan, T. Sun, and K. T. V. Grattan, "Long period grating-based humidity sensor for potential structural health monitoring," *Sensors Actuators, A Phys.*, vol. 148, pp. 57–62, 2008, doi: 10.1016/j.sna.2008.07.015.

[38] H. Tsuda and K. Urabe, "Characterization of long-period grating refractive index sensors and their applications," *Sensors*, vol. 9, no. 6, pp. 4559–4571, 2009, doi: 10.3390/s90604559.

[39] W. J. Bock, C. Jiahua, P. Mikulic, and T. Eftimov, "A novel fiber-optic tapered long-period Bragg grating sensor for pressure monitoring," *IEEE Trans. Instrum. Meas.*, vol. 56, no. 4, pp. 1176–1180, 2007, doi: 10.1109/TIM.2007.899904.

[40] X. W. Zhao and Q. Wang, "Mini review: Recent advances in long period fiber grating biological and chemical sensors," *Instrum. Sci. Technol.*, vol. 47, no. 2, pp. 140–169, 2019, doi: 10.1080/10739149.2018.1493499.

[41] J. M. P. Coelho, C. Silva, M. Nespereira, M. Abreu, and J. Rebordão, "Writing of Long Period Fiber Gratings Using CO2 Laser Radiation," *Adv. Opt. Fiber Technol. Fundam. Opt. Phenom. Appl.*, pp. 287–314, Feb. 2015, doi: 10.5772/59153.

[42] A. M. Vengsarkar, P. J. Lemaire, J. B. Judkins, V. Bhatia, T. Erdogan, and J. E. Sipe, "Long period fiber gratings as band-rejection filters," *J. Light. Technol.*, vol. 14, no. 1, pp. 58–65, 1996, doi: 10.1109/50.476137.

[43] B. Li, L. Jiang, S. Wang, H. L. Tsai, and H. Xiao, "Femtosecond laser fabrication of long period fiber gratings and applications in refractive index sensing," *Opt. Laser Technol.*, vol. 43, no. 8, pp. 1420–1423, 2011, doi: 10.1016/j.optlastec.2011.04.011.

[44] M. L. von Bibra, A. Roberts, and J. Canning, "Fabrication of long-period fiber gratings by use of focused ion-beam irradiation," *Opt. Lett.*, vol. 26, no. 11, pp. 765–767, 2001, doi: 10.1364/OL.26.000765.

[45] C. Colaço, P. Caldas, I. Del Villar, R. Chibante, and G. Rego, "Arc-induced long-period fiber gratings in the dispersion turning points," *J. Light. Technol.*, vol. 34, no. 19, pp. 4584–4590, 2016, doi: 10.1109/JLT.2016.2540678.

[46] R. Oliveira, L. M. Sousa, A. M. Rocha, R. Nogueira, and L. Bilro, "UV inscription and pressure induced long-period gratings through 3D printed amplitude masks," *Sensors*, vol. 21, no. 6, 2021, doi: 10.3390/s21061977.

[47] S. H. Shi, X. J. Zhou, Z. Y. Zhang, L. Lan, C. Yin, and Y. Liu, "Fiber-optic solution concentration sensor based on a pressure-induced long-period grating in a composite waveguide," *Chinese Phys. Lett.*, vol. 29, no. 9, p. 094206, 2012, doi: 10.1088/0256-

307X/29/9/094206.
[48] I. Torres-Gómez, D. E. Ceballos-Herrera, and K. M. Salas-Alcantara, “Mechanically-induced long-period fiber gratings using laminated plates,” *Sensors*, vol. 20, no. 9, 2020, doi: 10.3390/s20092582.
[49] C. Y. Lin, L. A. Wang, and G. W. Chern, “Corrugated long-period fiber gratings as strain, torsion, and bending sensors,” *J. Light. Technol.*, vol. 19, no. 8, pp. 1159–1168, 2001, doi: 10.1109/50.939797.
[50] C. Y. Lin, G. W. Chern, and L. A. Wang, “Periodical corrugated structure for forming sampled fiber Bragg grating and long-period fiber grating with tunable coupling strength,” *J. Light. Technol.*, vol. 19, no. 8, pp. 1212–1220, 2001, doi: 10.1109/50.939803.
[51] M. Vaziri and C. L. Chen, “Etched Fibers as Strain Gauges,” *J. Light. Technol.*, vol. 10, no. 6, pp. 836–841, 1992, doi: 10.1109/50.143084.
[52] C. Y. Lin and L. A. Wang, “Loss-tunable long period fibre grating made from etched corrugation structure,” *Electron. Lett.*, vol. 35, no. 21, pp. 1872–1873, 1999, doi: 10.49/el:19991143.
[53] C.-C. Chiang, H.-J. Chang, and J.-S. Kuo, “Novel fabrication method of corrugated long-period fiber gratings by thick SU-8 photoresist and wet-etching technique,” *J. Micro/Nanolithography, MEMS, MOEMS*, vol. 9, no. 3, p. 033007, 2010, doi: 10.1117/1.3478238.
[54] B. S. Finn, *City of Light: The Story of Fiber Optics (review)*, vol. 43, no. 1. 2002.
[55] J. Hecht, *Understanding Fiber Optics*, 5th editio. Laser Light Press, 2015.
[56] H. Kogelnik, “Theory of Optical Waveguides,” *Integr. Opt.*, pp. 33–52, 2009, doi: 10.1007/b98730_3.
[57] P. M. Tracey, “Intrinsic Fiber-Optic Sensors,” *IEEE Trans. Ind. Appl.*, vol. 27, no. 1, pp. 96–98, 1991, doi: 10.1109/28.67537.
[58] L. Bansal and M. El-Sherif, “Intrinsic optical-fiber sensor for nerve agent sensing,” *IEEE Sens. J.*, vol. 5, no. 4, pp. 648–655, 2005, doi: 10.1109/JSEN.2005.850991.
[59] G. Betta and A. Pietrosanto, “An intrinsic fiber optic temperature sensor,” *IEEE Trans. Instrum. Meas.*, vol. 49, no. 1, pp. 25–29, 2000, doi: 10.1109/19.836303.
[60] Z. Huang, Y. Zhu, X. Chen, and A. Wang, “Intrinsic Fabry-Pérot fiber sensor for temperature and strain measurements,” *IEEE Photonics Technol. Lett.*, vol. 17, no. 11, pp. 2403–2405, 2005, doi: 10.1109/LPT.2005.857236.
[61] S. J. Mihailov, “Fiber bragg grating sensors for harsh environments,” *Sensors*, vol. 12, pp. 1898–1918, 2012, doi: 10.3390/s120201898.
[62] S. W. James and R. P. Tatam, “Optical fibre long-period grating sensors: Characteristics and application,” *Meas. Sci. Technol.*, vol. 14, no. 5, pp. 49–61, 2003, doi: 10.1088/0957-0233/14/5/201.
[63] M. Rajibul Islam, M. Mahmood Ali, M. H. Lai, K. S. Lim, and H. Ahmad, “Chronology of fabry-perot interferometer fiber-optic sensors and their applications: A review,” *Sensors*, vol. 14, no. 4, pp. 7451–7488, 2014, doi: 10.3390/s140407451.
[64] K. Wang *et al.*, “Advances in Optical Fiber Sensors Based on Multimode Interference (MMI): A Review,” *IEEE Sens. J.*, vol. 21, no. 1, pp. 132–142, 2020, doi: 10.1109/JSEN.2020.3015086.
[65] L. B. Soldano and E. C. M. Pennings, “Optical multi-mode interference devices based on self-imaging: principles and applications,” *J. Light. Technol.*, vol. 13, no. 4, pp. 615–627, 1995, doi: 10.1109/50.372474.
[66] M. Silva-Lopez *et al.*, “Optical Sensing Using Fiber-Optic Multimode Interference

Devices: A Review of Nonconventional Sensing Schemes," *17th Int. Conf. Opt. Fibre Sensors*, vol. 5855, pp. 202–05, 2005, doi: 10.1117/12.623789.
[67] G. B. Hocker, "Fiber-optic sensing of pressure and temperature," *Appl. Opt.*, vol. 18, no. 9, pp. 1445–1448, 1979, doi: 10.1364/ao.18.001445.
[68] T. Erdogan, "Fiber grating spectra," *J. Light. Technol.*, vol. 15, no. 8, pp. 1277–1294, 1997, doi: 10.1109/50.618322.
[69] R. Oliveira, R. Nogueira, and L. Bilro, "3D printed long period gratings and their applications as high sensitivity shear-strain and torsion sensors," *Opt. Express*, vol. 29, no. 12, pp. 17795–17814, 2021, doi: 10.1364/oe.427387.
[70] P. Kiiveri *et al.*, "Refractive index profiles and propagation losses in bent optical fibers," *Opt. Eng.*, vol. 61, no. 12, pp. 1–15, 2022, doi: 10.1117/1.oe.61.12.126106.
[71] E. G. P. Pachon, M. A. R. Franco, and C. M. B. Cordeiro, "Spectral bandwidth analysis of high sensitivity refractive index sensor based on multimode interference fiber device," *OFS2012 22nd Int. Conf. Opt. Fiber Sensors*, vol. 8421, pp. 1–4, 2012, doi: 10.1117/12.969928.
[72] T. C. Poulter, C. Ritchey, and C. A. Benz, "The effect of pressure on the index of refraction of paraffin oil and glycerine," *Phys. Rev.*, vol. 41, pp. 366–367, 1932, doi: 10.1103/PhysRev.41.366.
[73] L. A. Wang, C. Y. Lin, and G. W. Chern, "A torsion sensor made of a corrugated long period fibre grating," *Meas. Sci. Technol.*, vol. 12, no. 7, pp. 793–799, 2001, doi: 10.1088/0957-0233/12/7/307.
[74] L. Cai, X. Ai, and Y. Zhao, "A displacement sensor based on balloon-like optical fiber structure," *Sensors Actuators A Phys.*, vol. 338, 2022, doi: 10.1016/j.sna.2022.113469.